Exploring Chemistry and Additive Manufacturing Design Spaces: A Perspective on Computationally-Guided Design of Printable Alloys

Sofia Sheikh[a], Brent Vela[a], Vahid Attari[a], Xueqin Huang[a], Peter Morcos[a], James Hanagan[a], Cafer Acemi[a], Ibrahim Karaman[a], Alaa Elwany[a,b], Raymundo Arróyave[a,b,c]

[a]*Department of Materials Science and Engineering, Texas A&M University, College Station, TX, USA*

[b]*Department of Industrial and Systems Engineering, Texas A&M University, College Station, Texas, USA*

[c]*Department of Mechanical Engineering, Texas A&M University, College Station, Texas, USA*

Abstract

Additive manufacturing (AM), especially Laser Powder-Bed Fusion (L-PBF), provides alloys with unique properties, but faces printability challenges like porosity and cracks. To address these issues, a co-design strategy integrates chemistry and process indicators to efficiently screen the design space for defect-free combinations. Physics-based models and visualization tools explore the process space, and KGT models guide microstructural design. The approach combines experiments, databases, deep learning models, and Bayesian optimization to streamline AM alloy co-design. By merging computational tools and data-driven techniques with experiments, this integrated approach addresses AM alloy challenges and drives future advancements.

Keywords: Additive Manufacturing, Lack of Fusion, Balling, Keyholing, Printability

List of Abbreviations and Symbols

Abbreviation/Symbol	Definition	**Abbreviation/Symbol**	Definition
α	Thermal Diffusivity	β	Solidification Shrinkage
ΔH	Specific Enthalpy	η	Alloy Laser Absorptivity
κ	Thermal Conductivity	ρ	Density
AC	Air Cooling	**AFE**	Automatic Feature Generation
AFLOW	Automatic-Flow for Materials Discovery	**AMMD**	Additive Manufacturing Materials Database
AM	Additive Manufacturing	**A**	Laser Absorptivity Coefficient
BN	Bayesian Networks	**BO**	Bayesian Optimization
C_P	Effective Heat Capacity	**CALPHAD**	Calculation of Phase Diagrams
CBFV	Composition-Based Feature Vector	**CEP**	Crude Estimation of Property
CET	Columnar-to-Equiaxed	**CDR**	Clustered Discriminant Regression
CNN	Convolutional Neural Network	**Comp.**	Composition
$\mathbf{D}_k$	Melt Pool Depth in Keyhole Mode	**DED**	Direct Energy Deposition
DFS	Deep Feature Synthesis	**DFT**	Density Functional Theory

Continued on next page

*Corresponding author email:sofiasheikh@tamu.edu

Abbreviation/Symbol	Definition	Abbreviation/Symbol	Definition
DNN	Deep Neural Network	**DOE**	Design of Experiments
DQN	Deep Q-Networks	D	Melt Pool Depth
d	Laser Beam Size	**ET**	Eagar-Tsai
FAIR	Findable, Accessible, Interoperable and Reusable	**FEM**	Finite Element Method
FGT	Feature Generation Tree	**GAN**	Generative Adversarial Network
G	Thermal Gradient	**GP**	Gaussian Process
G-S	Gladush and Smurov	**h**	Hatch Spacing
$\mathbf{H}_0$	Enthalpy at Substrate Temperature	$\mathbf{H}_L$	Enthalpy After Melting
HGP	Hierarchical Gaussian Process	**HTP**	High-Throughput
HV	Vickers Hardness	**ICME**	Integrated Computational Materials Engineering
Ke	Keyholing Number	**KGT**	Kurz-Giovanola-Trivedi
kNN	Kernel Nearest Neighbor	**kPCA**	Kernel Principal Component Analysis
L-PBF	Laser Powder Bed Fusion	**L**	Melt Pool Length
$\mathbf{L}_D$	Thermal Diffusion Depth	**LED**	Laser Energy Density
LIME	Local Interpretable Model-agnostic Explanations	**LOF**	Lack of Fusion
MI	Mutual Information	**ML**	Machine Learning
MICE	Multivariate Imputation by Chained Equations	**NED**	Normalized Energy Density
NN	Neural Network	**P**	Power
PCA	Principal Component Analysis	**PDF**	Primary Dendritic Arm Spacing
PFM	Phase Field Method	**q**	Heat Energy Input
$\mathbf{r}_0$	Laser Beam Spot Radius	**R**	Solidification Velocity
RFECV	Recursive Feature Elimination with Cross Validation	**RNN**	Recurrent Neural Networks
ROM	Rule-of-Mixtures	**SG**	Scheil-Gulliver
SHAP	Shapley Additive Explanations	**SISSO**	Sure Independence Screening and Sparsifying Operator
SRCC	Spearman Rank Correlation Coefficient	**T**	Temperature at time, t
$\mathbf{T}_0$	Substrate Temperature	$\mathbf{T}_b$	Boiling Temperature
$\mathbf{T}_L$	Liquidus Temperature	$\mathbf{T}_S$	Solidus Temperature
t	powder layer thickness	**t-SNE**	t-distributed Stochastic Neighbor Embedding
UMAP	Uniform Manifold Approximation and Projection	**v**	Laser Scanning Speed
VAE	Variational AutoEncoder	**WC**	Water Cooling
W	Melt Pool Width		

1. Introduction

In recent years, additive manufacturing (AM) has gained significant traction in both industrial and academic sectors, owing to its numerous benefits when compared to conventional subtractive manufacturing methods. Notably, AM excels in enabling the production of components with complex geometries, lightweight designs, and overall cost-effectiveness in the manufacturing process [1–3]. Currently, the two prominent AM technologies used to fabricate metallic products are Direct Energy Deposition (DED) [4] and Laser Powder Bed Fusion (L-PBF) [5]. DED is a method that melts a stream of metallic powder or wire and deposits it on underlying layers/substrates [6]. L-PBF is a method that successively melts the powder, layer by layer, to fuse the layers [7]. While both methods have pros and cons, the scope of this work is limited to L-PBF.

Laser Powder Bed Fusion (L-PBF) method in additive manufacturing (AM) is capable of producing alloys and components with superior characteristics. For example, AM-processed alloys have been shown to have unique microstructures [8, 9], and properties that, in some cases, exceed those of the same alloy when cast or wrought [10–12]. However, in many cases, the resultant microstructures are ridden with defects such as porosity, cracks, and residual stresses. Therefore, a key challenge in designing AM is to understand (and exploit) the Process-Structure-Property-Performance (PSPP) relationships for various materials and processing conditions. By understanding how the physical phenomena drive the PSPP relationships in AM, easily printed alloys with tailored microstructures can be designed. Once achieved, AM processing can be used to tune the microstructure, which affects the properties, which, in conclusion, dictates the performance of the part [13–15].

To establish PSPP linkages for reliably printing high-quality metallic parts, the L-PBF processing parameters must first be tuned to avoid porous microstructures. Porosities are microstructural defects that are common in metal AM and have detrimental effects on the final performance of the manufactured part. These porosity defects can be grouped into three primary categories: lack-of-fusion (LOF), keyholing, and balling [16]. Lack-of-fusion porosity occurs due to insufficient energy input such that the previous layer remelts to bond to the current layer or when there is a lack of overlap between adjacent tracks due to a large powder layer thickness or a large hatch spacing [17]. Keyhole-induced pores occur due to the excessive energy density, leading to evaporation and high recoil pressure on the surface of the melt pool and, subsequently, gas entrapment [18]. Balling is caused by a reduction in the wettability of the molten liquid on the substrate as a result of insufficient energy input and high surface energy [19].

In addition to porosity, other defects that can occur during the AM process include thermally induced distortion and cracking. Distortion is caused by the high residual stresses arising from the large thermal gradients produced during printing [20], while cracking can be caused by two different mechanisms. Hot cracking occurs during the final stages of solidification when the melt pool is semisolid [21]. In this semisolid state, the material is fragile and vulnerable to stresses induced by solidification shrinkage. Another type of cracking is thermal shock-induced cracking [22]. This mode of cracking is common in brittle materials such as W [23]. Thermal shock-induced cracking occurs when large temperature gradients generated during the AM process cause the accumulation of thermal stresses. If the material is ductile, the material can deform elastically to accommodate these stresses [24]; however, if the material is brittle (as in the case of W), the thermal stress is alleviated by the formation of microcracks in the recently solidified melt pool.

Initial works concerning L-PBF focused on tuning processing parameters to print 'legacy alloys' that were originally designed for processing routes besides L-PBF. For example, legacy alloys 316 and 718 stainless steel have been shown to be susceptible to keyhole porosity and thermal cracking during L-PBF [25]. Likewise, while it was possible to achieve defect-free prints of AF96, the window of viable processing parameters is narrow [26]. Later work explored the potential of tailoring alloys to be amenable to AM [27, 28], however, these works addressed single-objective design schemes that optimized only alloy printability.

In work under preparation [29], we conducted an *in − silico* chemistry-process co-design campaign, optimizing performance and printability simultaneously; however, such frameworks still need to be validated experimentally. We believe that alloy design must consider the chemistry and processing design spaces simultaneously. Furthermore, alloy design for AM can not be myopically focused on printability. However, it should be multi-objective to find alloy-process pairs with optimal properties and processability.

Although chemistry-process co-design is promising, there are challenges that must first be overcome to realize experimental co-design campaigns. If one considers the processing space associated with a single alloy, there are hundreds of parameters that affect the resulting print, including but not limited to power, scan speed, hatch spacing, scan strategies, powder layer thickness, and powder morphology [30, 31]. When a chemistry space is also considered, the union of these design spaces quickly becomes vast and difficult to explore using traditional means—- more sophisticated and resource-efficient approaches would be necessary [32].

In order to co-design in the vast chemistry-process L-PBF design space, Integrated Computational Materials Engineering (ICME) methods are needed. Computational tools such as Machine Learning (ML) frameworks, thermodynamic databases, and high-fidelity physics-based simulations have been implemented to establish linkages along the PSPP chain [33, 34]. Based on the available literature and our experience with high-throughput (HTP) ~~HTP~~ alloy design, our perspective is that the ideal AM design campaign is as shown in Figure 1.

In this work, we offer insights about the crucial role that computational models play in establishing PSPP linkages and fostering the discovery of innovative materials for AM. While ICME methods have been employed independently in alloy design, we advocate their integration into a comprehensive closed-loop framework. Our perspective aligns with the understanding that design of AM artifacts should consider both chemistry and processing conditions [11, 35, 36]. Building on this foundation, we emphasize the dual-focus approach required for effective alloy design in AM, addressing both the chemistry and processing design spaces concurrently using a composition-agnostic constrained optimization methodology, shown in Figure 1. To create an efficient strategy, the initial step involves filtering this design space using cost-effective models (Figure 1a), followed by a deeper exploration of computational studies to assess printability and microstructure (Figure 1b and c). Once potential alloy-process candidates have been identified, empirical tests can be conducted. The experimental data can then be organized within databases (Figure 1d), which simplifies the access of the experimental data to compare them with the predictions of the model in order to assess the accuracy of the model. The experimental data can then be analyzed using ML models, with subsequent experiments informed by Bayesian optimization (Figure 1e). This iterative approach provides a viable solution to the challenging task of alloy design for AM.

2. Physics-driven Approaches for Additive Manufacturing

To successfully identify alloys suitable for AM printing, a deep understanding of the PSPP relationships is crucial. These relationships are the result of intricate phenomena resulting from the interplay between the energy source, the feedstock, and the local environment. These phenomena are shaped by controllable AM process parameters and unpredictable factors, such as varying cooling rates due to local geometries and heat transfer processes. The localized thermal histories and subsequent phase changes during deposition dictate the final macro- and microstructures, which in turn influence the material properties. Relying exclusively on experimental or data-driven methods is insufficient given the complexity of the problem and the (usual) sparsity in the available data. A comprehensive approach that leverages our understanding of the core physical phenomena during AM is imperative to ensure optimal printing outcomes [14, 41, 42].

Porosity stands out as a crucial microstructural factor with a significant impact on the performance of printed parts [16]. Specifically, the presence of porosity has a notable influence on the local yield surface in AM metal parts [43]. On the other hand, by (almost) completely eliminating porosity from AM specimens it is possible to fabricate parts that match—or surpass—the properties of wrought counterparts [44]. As detailed in Section 1, defects resulting from porosity can be categorized into keyholing, balling, and lack-of-fusion pores. To ensure the fabrication of high-quality products, it is vital to understand the physical processes leading to porosity formation in different regimes within the AM process space.

For example, Tang et al. introduced a geometry-based model to predict the onset of porosities caused by LOF [45]. Khairallah et al. [46] constructed a powder-scale model that simulated the physical mechanisms involved in the formation of pores. The study highlighted the importance of recoil pressure, the Marangoni effect, and solidification as the underlying mechanism for pore formation. These physics-based methods are useful; however, because of the significant computational demands of these physics-based methods, there is a need to adapt their application for HTP alloy design in AM. Here, we present a perspective on using physics-based indicators and visualization models that can be used to develop fast-acting physics-based approaches to evaluate the propensity for the formation of various printing defects for a given alloy composition.

Physics-Based Indicators: For HTP design, indicators can be used to evaluate the chemistry and process space to determine which compositions are more printable or easier to print relative to other compositions in the process space. This allows one to perform a initial screening of the design space and reduce the the number of potential alloy-process candidates. After this cheap screening, more expensive thermal modeling can be conducted on the remaining candidates, as we discuss in Section 2.2.

Visualizing the Printability of Alloy: After identifying potentially printable alloys, thermal modeling can be conducted in order to assess the printability of an alloy at various processing conditions. These results are often displayed in printability maps. Printability maps, also referred to as processing maps, are a 2D visualization tool that allows for an insight into the processing space for regions where the alloy is defect-free. Different methods have been utilized to create such maps to aid in determining optimal process conditions for experiments.

2.1. Physics-based Indicators

Indicators (also referred to as criteria or indices) are important for HTP design approaches. Indicators are quantities that are correlated with a property of interest but do not necessarily predict it. Typically, indicators are easy-to-compute descriptors associated with candidate designs. In the context of alloy design for AM, indicators are important as they can be used to rapidly screen vast chemical, processing, and performance spaces in search for useful (e.g. high yield strength), printable (e.g. crack-resistant) alloys and their corresponding optimal processing conditions.

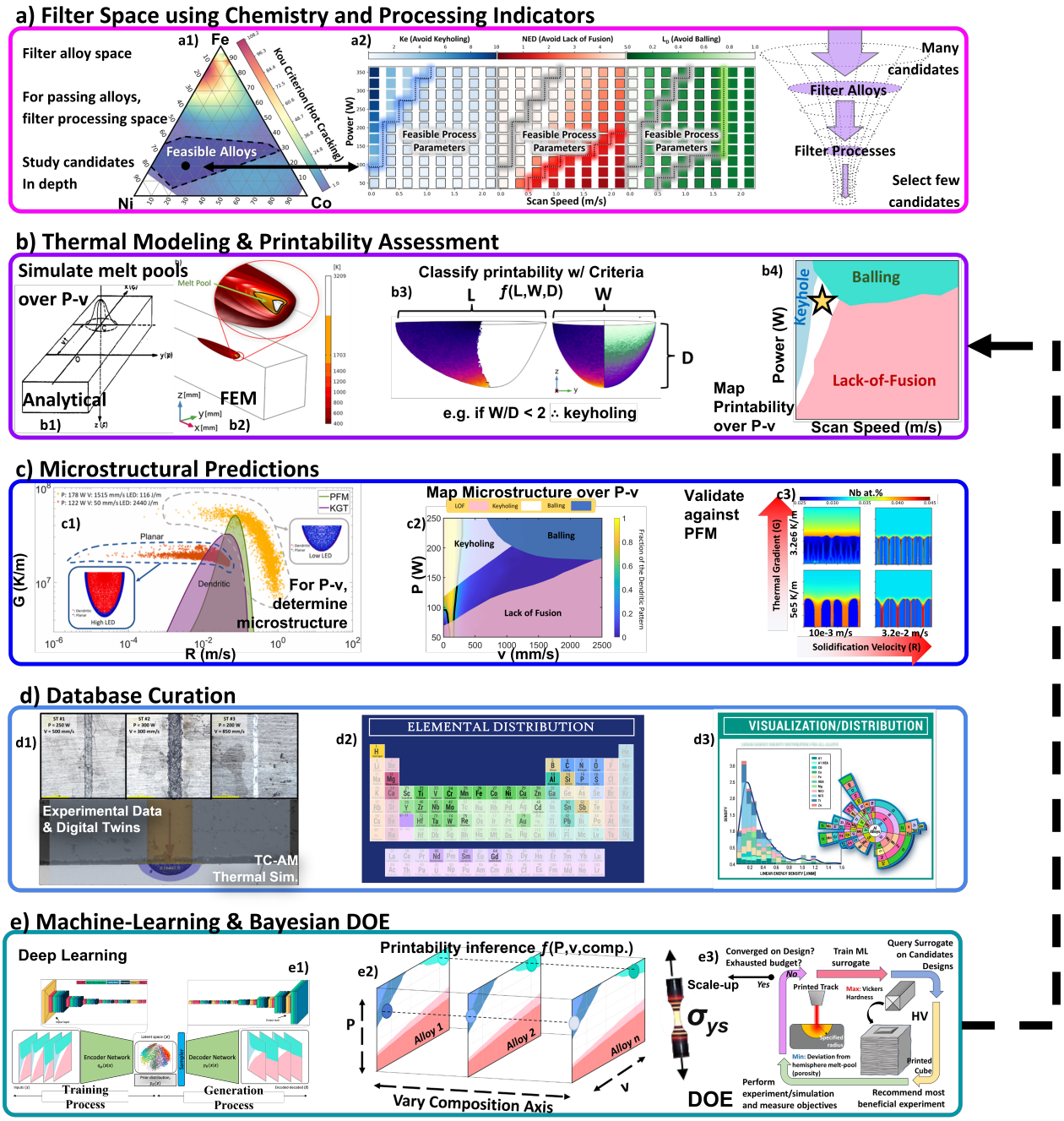

Figure 1: a) Illustration of how *fast − acting* printability indicators enable a first-pass filtering of the chemistry-process space. a1) An indicator is used to find alloys resistant to hot-cracking. a2) For a single alloy, the processing space is filtered using 3 printability indicators. Such screening ensures that resources are allocated to alloy-process pairs with a high likelihood of yielding defect-free prints. b) Next, these down-selected alloy-process pairs are further assessed for printability. A thermal model simulates the dimensions of the melting pool for a grid of powers and velocities. b1) This thermal model can be analytical [Reproduced from Ref. [37]] or b2) FEM-based [Reproduced from Ref. [16]]. b3) Melt pool dimensions are then used to evaluate printability criteria [Reproduced from Ref. [38]]. b4) If a processing condition is classified as leading to the formation of a defect, it is marked on the printability map. c1) For various laser powers and scan speeds the as-print microstructure can be predicted using solidification theories that are based on thermal gradients and solidification velocities [Reproduced from Ref. [39]] c2) These microstructural predictions can also be mapped on the laser power-scan speed space [Reproduced from Ref. [39]]. c3) These predictions can be validated against high-fidelity PFMs. d) Once the alloy-process combinations that are likely to yield prints free of cracks and porosity with desired microstructures have been identified, computationally, experiments can be performed. The resultant experimental data should be curated in databases. e1) Once a database has been curated, ML analysis on printability maps can be performed [The ML model architecture is reproduced from Ref. [40]]. e2) These models can be used to predict printability as a function of laser power, scan speed, and composition. e3) Bayesian analysis can be used to design a subsequent set of experiments. P: Laser Power. V: Scan Speed. FEM: Finite element method. PFM: Phase field model. L: Length. W: Width. D: Depth. G: Thermal Gradient. R: Solidification velocity. DOE: Design of Experiments. Comp.: Composition.

Many composition-based indicators are available that can be used to select alloys amenable to AM. For example, to screen for solidification defects, multiple criteria have been derived from the Scheil-Gulliver curve (SG-curve). Specifically, the solidification range of the SG-curve has been minimized during alloy design to mitigate hot tearing and compositional microsegregation [47–50]. Similarly,

Clyne and Davies [51], Rappaz-Drezet-Gremaud [52], Djurdjevic and Huber [53], Kou [54], Tang [21], and Easton [55], and Suyitno [56] have developed multiple criteria for hot cracking.

The utility of these hot-cracking criteria varies. For example, the Suyitno criterion requires difficult-to-measure quantities such as Young's modulus of the semisolid mush zone, surface tension between liquid and solid, and permeability of the mush, thus limiting its widespread adoption. On the other hand, indicators such as the Kou criterion and the Clyne and Davies criterion rely on easy-to-reach quantities such as the Scheil-Gulliver curve (which can be queried in an HTP manner using Thermo-Calc's TC-Python API). The most recent hot-cracking indicators are from Tang et al. [21]. This indicator is a modification of the Kou indicator, but accounts for solidification shrinkage (β). It is our perspective that the Kou-Tang indicator is important as it accounts for solidification gradient (non-mechanical aspect) and solidification shrinkage (mechanical aspect). All quantities required for this indicator can be queried in an HTP manner using thermodynamic software, making it a useful indicator. To demonstrate this ease of querying, Figure 2 a shows these two criteria queried for 299 alloys in the FeNiCo alloy space.

Most process-based indicators give insight into an alloy's susceptibility to form porosity defects (i.e balling, keyholing and LOF) at specific processing conditions. Gan et al. [57] proposed two dimensionless quantities that are correlated to keyholing and LOF. Specifically, the keyholing number (Ke) which captures the ratio of the absorbed laser energy density to the volumetric melting enthalpy. The term Ke is defined as $\frac{\eta P}{(T_L - T_0)\pi\rho C_p \sqrt{\alpha v r_0^3}}$ where η is laser absorptivity, P is laser power, ρ is density, C_p is the effective heat capacity, T_L is the liquidus temperature, T_0 is the substrate temperature, α is the thermal diffusivity, v is laser scan speed, and r_0 is the beam radius. Likewise, the normalized energy density (NED) number captures the ratio of effective energy density within the powder bed to the energy density required to bring the alloy to its melting point [57]. Specifically, NED is the ratio of the normalized energy input to the product of the normalized velocity and dimensionless layer thickness [58], simplified as $\frac{\eta P}{vt\rho C_p (T_L - T_0)}$ where h is the hatch spacing and t is the powder layer thickness. Rankouhi et al. [59] used Buckingham's Π-theorem to generate two dimensionless numbers that provide an estimation of defect mode (LOF or keyholing) and relative density for a wide range of materials. In the case of balling, several authors [60, 61] note that the ratio between thermal diffusivity and the product of laser scan speed and laser spot size, $L_D = \sqrt{\alpha/(v r_0)}$, is indicative of thermal diffusion depth, i.e., when $L_D < 1$ the melt pool is shallow and elongated, which can lead to balling. Zhou et al. [62] discovered that the balling in W could be explained by the competition between the spread and solidification of a melt droplet over a metal substrate. Using this insight, Vela et al. [28] developed an indicator based on the ratio between the characteristic spreading times and wetting time of liquid alloy melts.

The advantage of the indicators above is that they only rely on thermophysical properties that can be queried in an HTP manner from a CALPHAD software such as Thermo-Calc. To demonstrate this $ease - of - query$ we have deployed these indicators throughout the chemistry-process space for the FeNiCo system as shown in Figure 2. Chemistry-based indicators such as the freezing range and the Tang-Kou criteria are plotted over the ternary chemistry space, as shown in Figure 2a. However, every alloy within this chemistry space has an associated processing space, as shown in Figure 2b. When considering indicators that are functions of AM processing parameters, we visualize these indicators over the process space. Specifically, in Figure 2b, the blue squares represent Ke (decrease indicator to avoid keyholing). The red crosses represent the NED (increase indicator to avoid LOF). The green circles represent the diffusion length scale (minimize to avoid balling).

Furthermore, metrics in the processing space can be mapped to those in the chemistry space. For instance, a summation over the indicators in the processing space can condense these indicators into a single metric that can be used to rank the intrinsic printability of an alloy. In Figure 2b the Ke, NED, and L_D are summed across a given power-velocity grid. These sums can then be plotted over a chemistry space, as shown in Figure 2a. For example, $\sum_P \sum_v$NED is highest for Ni-rich alloys, indicating that they may be more susceptible to LOF defects. Likewise, Fe-rich alloys have higher values for $\sum_P \sum_v$Ke, indicating suceptibility to keyholing. To the authors' knowledge, this is the first time these indicators have been queried in an HTP manner for arbitrary alloys and visualized in the union of alloy and processing design spaces.

To corroborate the trends in Figure 2, consider the following: NED is proportional to melting temperature, laser associativity, effective heat capacity, and density, expressed as $NED \propto \eta/(\rho C_p T_L)$. For Fe, this term is estimated to be 3.8E-11, while for Ni, it is 3.5E-11, indicating that Ni is more susceptible to LOF, as illustrated in Figure 2. Laser associativity is estimated from thermal resistivity via Drude's theory [63]. The absorptivity for Ni and Fe are approximately the same. The effective heat capacity is calculated as the difference between enthalpy at the substrate temperature and the enthalpy just after melting divided by the difference between the substrate temperature and the liquidus temperature: $C_p = \frac{H_L - H_0}{T_L - T_0}$. All relevant properties are estimated using the TCHEA5 CALPHAD database and are shown in Table 2.

Likewise, metrics defined in the 'solidification space'— i.e. the domain of thermal gradients (G) and solidification velocities (R) as shown in Figure 2c — can be mapped to the alloy space. As detailed in Section 3, HTP implementations of solidification models such as the Kurz-Giovanola-Trivedi (KGT) model can be used to derive microstructual indicators. Once such indicator is the area of the dendritic region in the solidification space, represented by the yellow region in Figure 2c. The larger the dendritic area, the more combinations of Gs and Rs will result in a dendritic microstrucutre. In Figure 2c, the area of the dendtritic region in

	Fe	Ni
Melting Temperature (T_L)	1538°C	1455°C
Density (ρ)	7.87 kg/m^3	8.9 kg/m^3
Effective Heat Capacity (C_p)	869 J/kg/K	872 J/kg/K
Laser absorptivity (η)	0.4	0.4
$\eta/(\rho C_p T_L)$ =	3.8E-11	3.5E-11

Table 2: Relevant thermophysical properties for calculating the NED for Ni and Fe. These results indicate Ni is more difficult to melt than Fe, which is corroborated in Figure 2.

solidification space can be summed and used as an indicator to predict the tendency of an alloy to exhibit dendritic micostructures. These microstructural predictions are in agreement with other indicators. In Figure 2, the alloys with the highest dendritic tendency are also the alloys that have the largest solidification range and the largest tendency toward hot-cracking. This makes intuitive sense because the hot-cracking mechanism relies on dendritic solidification [64, 65]. Alloys with a large solidification range also exhibit a large non-planar solidification region in the G-R space. One limitation of this indicator is that it does not distinguish between the prevalence of columnar-dendritic and equiaxed-dendritic solidifications. This is important as columnar-dendritic solidification is far more susceptible to hot-cracking than equiaxed-dendritic solidification. A potential refinement to this G-R indicator would involve calculating the columnar-to-equiaxed transistion (CET) [66], overlaying CET and KGT maps in G-R space, and quantifying the area of columnar-dendritic solidification.

The indicators deployed in Figure 2, are not intended to be exhuastive. For example, the solidification range criteria is not applicable for CoCrFeNi as its hot-cracking mechanism is due to high thermal stress rates [67]. Instead, Figure 2 is meant to be illustrative of the importance of easy-to-query design metrics in the context of composition-agnostic AM alloy design frameworks. Other considerations we urge the AM community to consider during HTP filtering are as follows:

- Hot-cracking can potentially be avoided with via HTP inoculant design as demonstrated by Martin et al. [64]. The authors screened the following metrics in the inoculant space: thermodynamic stability in the desired alloy, minimization of lattice misfit between alloy and inoculate, and maximization of the similarity of atomic packing along matched crystallographic planes of alloy and inoculant. The designed inoculant promoted fine equiaxed grains, which are more resistant to hot-cracking than columnar grains.
- When it is known that the hot-cracking mechanism is due to thermal stress rates, as in the case of CoCrFeNi alloy [67], hot-cracking can be mitigated via segregation engineering. Specifically, if the solidification sequence is tuned, stable segregant phases with tuned molar volumes can offset the tensile stress between grains caused by solidification shrinkage, reducing the frequency of hot-cracking [68, 69]. Such calculations can be performed with Scheil simulations using CALPHAD software [68]. Specifically, Scheil simulations can be deployed to estimate the dendritic/interdentric composition, the solidification sequence of each region, and the molar volume change of each solidified region.
- We recommend using performance indicators to design high-performing printable alloys. Alloy design for AM cannot be myopic but must focus on high-performing alloys that are also printable. Such performance indicators could include HTP models/indicators for the stability of specific phases, avoidance of deleterious phases, strength, ductility, or density.

Regarding the limitations of this indicator-based alloy design scheme, it is essential to acknowledge the inherent risks associated with the use of screening models, as they may lead to misclassifications such as false positives or false negatives. Importantly, any misclassifications can be leveraged within a Bayesian closed-loop experimental campaign [32], as discussed in Section 5.3. In such campaigns, the learning process is iterative, allowing for adjustments and corrections to the model based on the insights gained from the identified "mistakes" or misclassifications. However, despite the potential for misclassification, we maintain that the criteria employed in our study remain valuable for guiding alloy design. We align with the positions stated in Ref [70]: "When data are limited, qualitative predictions that provide direction are more valuable than interpolative accuracy."

The major benefit of these indicators is the fact that they can be queried in a fast manner, which is ideal for HTP approaches. This is particularly important when considering the expense involved in constructing a printability map. In Section 2.2, we highlight a major bottleneck evaluating an alloy's printable window -the deployment of single-track simulations to predict melt pool dimensions, which are then used to generate printability maps. We take the perspective that these indicators should be used as a first-pass filter in order to discard alloy-process pairs that are likely not suitable for L-PBF AM. This approach enables the allocation of resources, such as expensive single-track and microstructural simulations, to more promising alloy-process pairs.

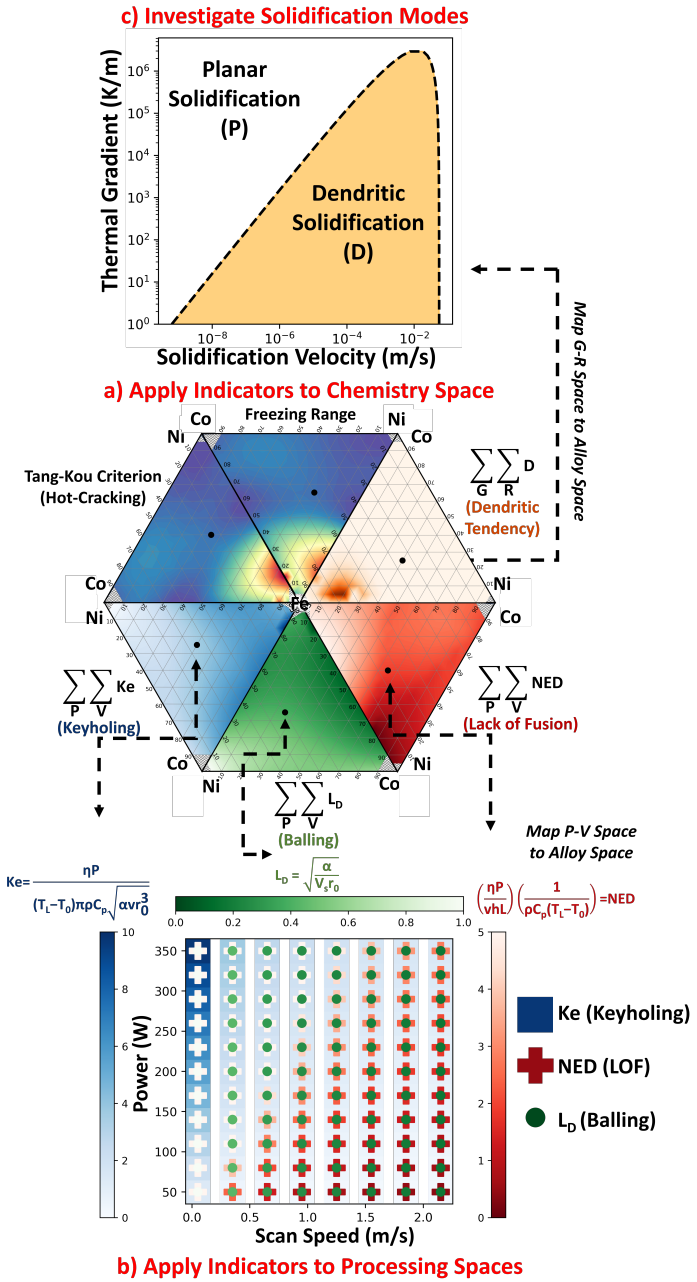

Figure 2: a) Various indicators are queried in the FeNiCo chemistry space. The hexagonal arrangement of the ternary diagram is for compactness and aesthetic purposes. b) Porosity defect indicators queried in the processing space associated with a single alloy in the FeNiCo chemistry space. The summation of these 3 defect indicators across the power-velocity space can be considered as a measure of an alloy's intrinsic tendency toward certain defects. c) The area of the dendritic region in the KGT map (G-R map) for a particular alloy. This indicator is highly correlated with indicators for hot-cracking, which makes sense as the hot-cracking mechanism itself is dependent on dendritic solidification [64, 65]. Ke: Keyholing Number. NED: Normalized Energy Density. L_D: Thermal Diffusion Depth. G: Thermal Gradient. R: Solidification Velocity. P: Power. V: Velocity.

2.2. *Visualizing the Printability of Alloys*

In L-PBF, a printability map provides invaluable insights into the optimal processing parameters for an alloy. While there are over 100 processing parameters associated with L-PBF that can potentially affect the quality of the final product [31], the most commonly varied parameters are laser power, scan speed, powder layer thickness, and beam size. Consequently, printability maps are typically functions of laser power and scan speed, while the powder layer thickness and beam size are specified constants. As depicted in Figures 8 and 4a, these maps treat the selection of processing parameters as a classification problem. The defined regions for the laser power-scan speed space are classified according to the underlying porosity defect mode—balling (green), LOF (pink), or keyholing (blue). The defect-free region, also called the printable region, remains uncolored.

Printability maps can be constructed through two primary methods: a data-driven approach or the utilization of computational models

calibrated with empirical data. In data-driven approaches, ML models are trained with experimental measurements for the melt pool dimensions obtained from single-track experiments. Alternatively, the boundaries of the defect regions can be delineated directly from the experimental data, bypassing the need for ML models. For example, Wilkinson et al. [71] and Wentai et al. [72] used a convolutional neural network model (CNN) trained with single tracks to construct the printability map of the Ti-6Al-4V alloy system. Zhang et al. [73] applied a support vector machine classifier to map the processing space using experimental data for $Ni_{51.2}Ti$. Meanwhile, Juechter et al. [74] established the keyhole and LOF boundaries for Ti-6Al-4V through direct analysis of experimental data, without invoking ML models.

Physics-driven methods for producing printability maps are gaining traction in the recent literature, with many studies leveraging analytical models. Childs et al. [75] used an uncalibrated analytical model to determine the printable region for H13 steel. In parallel, research by Zhang et al. [26, 76], Seede et al. [44, 77], and Shoukr et al. [78] utilized a calibrated Eagar-Tsai (ET) model to create printability maps for a range of alloys. Agrawal et al. [79] applied an analytical model to generate maps for six different alloy compositions and compared their predictions with experimental observations. This approach was further extended by the current authors [29] to allow HTP evaluations of printability within the Co-Cr-Fe-Mn-Ni HEA ('Cantor') system.

The methodology proposed by the current authors can be divided into three stages as shown in Figure 3: 1) calculating material properties, 2) predicting the geometry of the melt pool, and 3) constructing printability maps with various boundary conditions for the defined defect. This methodology is widely applicable in HTP contexts and has been thoroughly explored for various alloys [80]. It is noted that the material proprieties utilized throughout the proposed framework can be calculated using either Thermo-Calc or simple models such as the rule-of-mixtures (ROM).

To calculate the dimensions of the melt pool, the ET model is utilized. The ET model is considered one of the most acceptable and inexpensive analytical models in the AM community. It can predict the dimensions of the melting pool for a moving heat source with Gaussian beam distribution on a semi-infinite substrate, utilizing the Rosenthal equation, as detailed in Ref. [37]. Using the Green's function, precise predictions for the temperature distribution can be obtained using the following equation:

$$T - T_0 = \frac{1}{2}\int_{t'=0}^{t'=t} dT_{t'} = \frac{q}{\pi\rho C_p\sqrt{4\pi\alpha}}\int_{t'=0}^{t'=t}\left[\frac{(t-t')^{-\frac{1}{2}}}{2\alpha(t-t')+\sigma^2}e^{\left[-\frac{(x-vt')^2+y^2}{4\alpha(t-t')+2\sigma^2}-\frac{z^2}{4\alpha(t-t')}\right]}\right]dt' \tag{1}$$

In the above equation, T_0 is the initial temperature of the substrate, T is the calculated temperature at time t at any point with the coordinate of (x,y,x). Two categories of input parameters are used in the model, namely, process parameters and material properties. The process parameters are q, which denotes the heat energy input to the material calculated by multiplying the heat source power times the absorptivity of the material, v denotes the scanning speed, and α is the thermal diffusivity calculated by the following equation:

$$\alpha = \frac{\kappa}{\rho C_p} \tag{2}$$

The calculated melt pool width and depth agree well with the experimental measurements, especially when the process parameters fall in the region when the conduction mode occurs. However, at high linear energy densities; i.e., high laser power and low scanning speeds, where keyholing mode occurs, the ET model fails to predict the melt pool depth precisely. Therefore, a simple expression proposed by Gladush and Smurov [81] (referred to as the G-S model) can be applied to estimate the depth of the melt pool in the keyhole mode, as follows:

$$D_k = \frac{AP}{2\pi\kappa T_b} ln\left(\frac{d+\frac{\alpha}{v}}{d}\right) \tag{3}$$

where A is the laser absorptivity coefficient, P is the laser power, κ is the thermal conductivity, T_b is the boiling temperature , d is the laser beam size, v is the scanning speed.

This predicted melt-pool geometry can be used to predict the onset of certain porosity defects during L-PBF. The melt pool dimensions (L,W, and D) are predicted at various powers and velocities. The melt pool geometries are then fed to the defect criteria in Table 3. These criteria are functions of this geometry (and materials properties as in the case of KH2 and KH3). The prediction accuracy of the model can be assessed by treating the problem as 4 binary classification problems, where each region in the printability map corresponds to an independent classification problem [80]. Various alloys have been evaluated, including 316 stainless steel, AF96, Inconel 718, Ti-6Al-4V, Ni-5Nb, and NiTi alloys [29, 80]. In Figure 3, the printability map for $Ni_{51.2}Ti$ [reproduced from Ref. [80]]

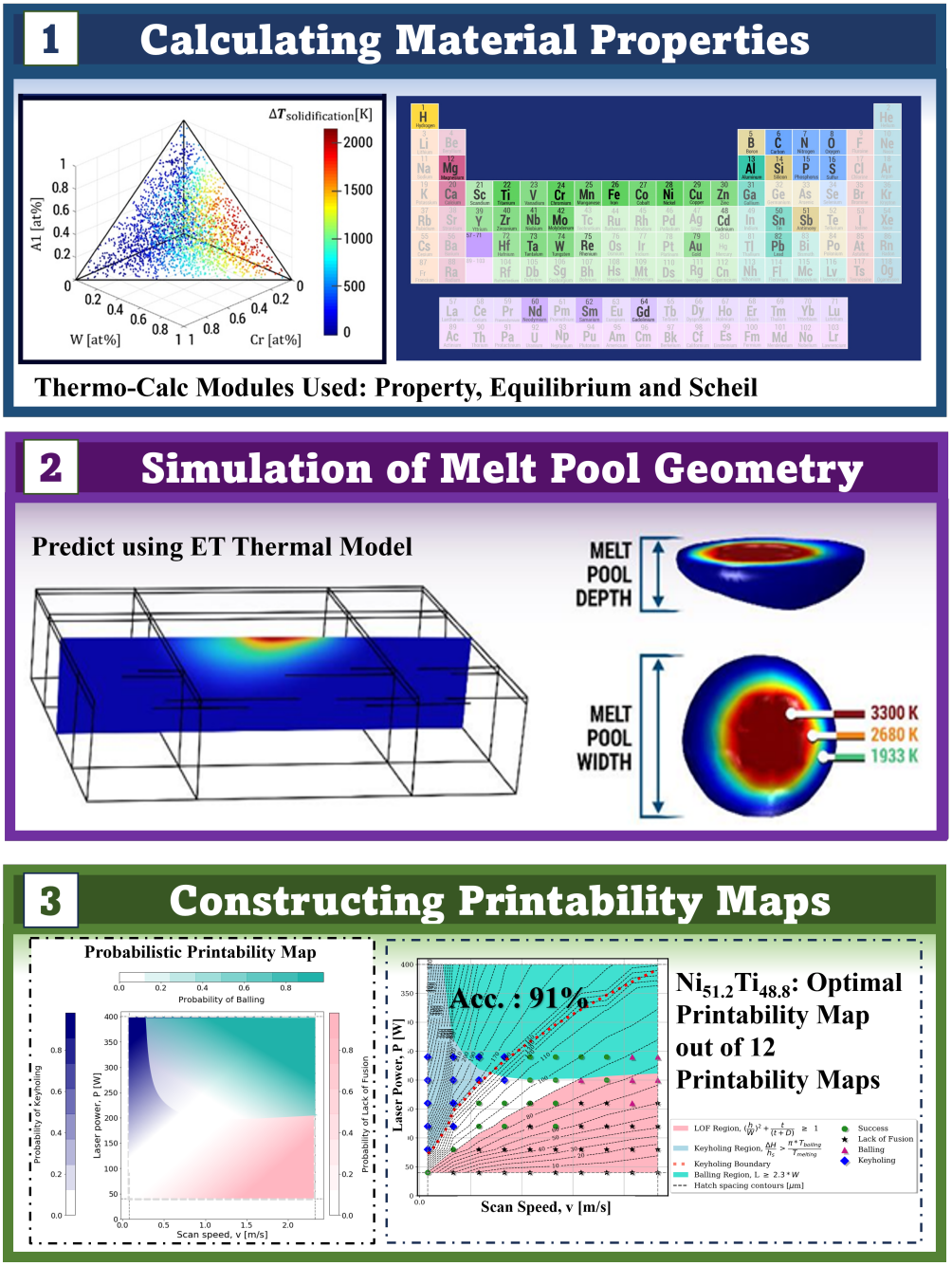

Figure 3: The computational framework is designed to predict printability maps in the HTP context for L-PBF. The initial step involves calculating material properties using either Thermo-Calc or simple material models. Some of these material properties are utilized as input parameters for the ET thermal model, which is employed in the framework's second step to predict the melt pool geometry. In the third step, a set of functions using both material properties and melt pool dimensions as input parameters is employed to define the boundaries for porosity-based defects, resulting in the generation of 12 printability maps. These criteria for defect boundaries encompass 2 criteria for lack of fusion (LOF), 2 for balling, and 2for keyholing. By comparing the predicted labels to experimental labels, the framework can produce probabilistic printability maps and benchmark criteria sets. The optimal printability map for $Ni_{51.2}Ti$ [reproduced from Ref. [80] had an accuracy of 91% highlights the applicability of the proposed methodology.

Defect Type	Label	Equation
Lack of Fusion	LOF1	$D \leq t$ [26]
	LOF2	$(\frac{h}{W})^2 + \frac{th}{th+D} \geq 1$ [82]
Balling	Ball1	$\frac{L}{W} \geq 2.3$ [16, 26]
	Ball2	$\frac{\pi W}{L} < \sqrt{\frac{2}{3}}$ [19]
Keyholing	KH1	$\frac{W}{D} \leq 2.0$ [16, 26]
	KH2	$\frac{\Delta H}{h_s} = \frac{AP}{\pi h_s \sqrt{\alpha \nu r_0^3}} > \frac{\pi T_b}{T_L}$ [61, 83]
	KH3	$Ke = \frac{\eta P}{(T_L - T_0)\pi \rho C_p \sqrt{\alpha \nu r_0^3}} > 6$ [57]

Table 3: The boundary conditions for each respective defect is defined and labeled. From the different combinations of these criteria, 12 printability maps can be generated. Using these criteria for $Ni_{51.2}Ti$, the optimal criteria combination was chosen when compared with experimental observation in Figure 3.

illustrates the applicability of the proposed framework. We note that the present framework accounts for uncertainty in the criteria used, and this uncertainty can in turn be used to construct probabilistic printability maps.

3. Microstructural Considerations in Additive Manufacturing

The properties and performance of parts fabricated via AM exhibit considerable variability, largely due to variations in the resulting microstructures [84, 85]. Microstructural variation, in turn, originates from the high variability in the local thermal histories. Wang et al. illustrated this by studying the effect of dynamic solidification conditions—under water cooling (WC) and air cooling (AC)—on the mechanical properties of Al–Mg–Sc–Zr alloys in L-PBF [86]. The high cooling rate in the WC case suppressed precipitation of primary $Al_3(Sc, Zr)$ particles by hindering the formation of nucleation sites for primary $Al_3(Sc, Zr)$ within the melt pool and promoted the secondary $Al_3(Sc, Zr)$ particles, which resulted in the increase of the yield strength of the alloy. Conversely, an equiaxed microstructure and low yield strength can be observed in AC conditions because of the relatively low cooling rates.

Traditional methods like phase field modeling (PFM) predicts microstructures under AM conditions. Karayagiz et al. introduced a framework for microstructure prediction in the Ni-Nb alloy system during laser powder bed fusion (L-PBF) using varying linear energy density (LED) [38]. They employed a finite element (FEM) thermal model with a moving heat source for local thermal history and a finite interface dissipation PFM for microstructure evolution. Low LED yields a planar microstructure due to high growth rates, while medium and high LED result in cellular/dendritic structures. These results were shown to be consistent with experiments.

Figure 4 shows a few examples of simulations of macro/micro-structural evolution under AM conditions. ~~Figure 4a [reproduced from Ref. [87]] shows the appearance of ripples on the molten track when using high laser power. They are caused by the Marangoni force when laser power is high, causing large temperature gradients around the laser spot, resulting in large gradients in surface tension, which drive the molten metal towards a certain direction.~~ Figure 4a reproduced from Ref. [88] shows the time evolution of grains in a polycrystalline material as the laser progresses, causing the grains to melt along the leading edge of the melt pool. Figures 4b, c and d shows the microstructure distribution predicted by an integrated model, which couples a FEM thermal model with a PFM, as proposed by Karayagiz et al. [38]. Figures 4b and c [reproduced from Ref. [89]] correspond to the predicted and experimental microstructure distribution, respectively, for a Ni-20 at% Cu binary alloy during AM processing. The two distributions (cell bottom) agree with each other. Figure 4d shows two example microstructures predicted by PFM: Planar and cellular. This work connects the processing parameter and the microstructure distribution. By avoiding ~~the~~ cellular ~~microstructure~~ and other non-planar solidification morphologies such as equiaxed and columnar dendritic, it is, in principle, possible to achieve a microstructure homogeneous in chemistry and reduce the need for post-process homogenization.

Phase-field models provide the means to establish the connections between process conditions and microstructures, but they are computationally expensive and thus impractical in the context of HTP exploration of alloy-process spaces. The KGT theory [90] identifies the range of thermal gradients (G) and solidification velocities (R) that result in the ~~absolute~~ stability of the planar liquid-solid interface. ~~When the liquid-solid interface is stable, planar solidification takes place, otherwise, cellular/dendritic growth occurs~~.

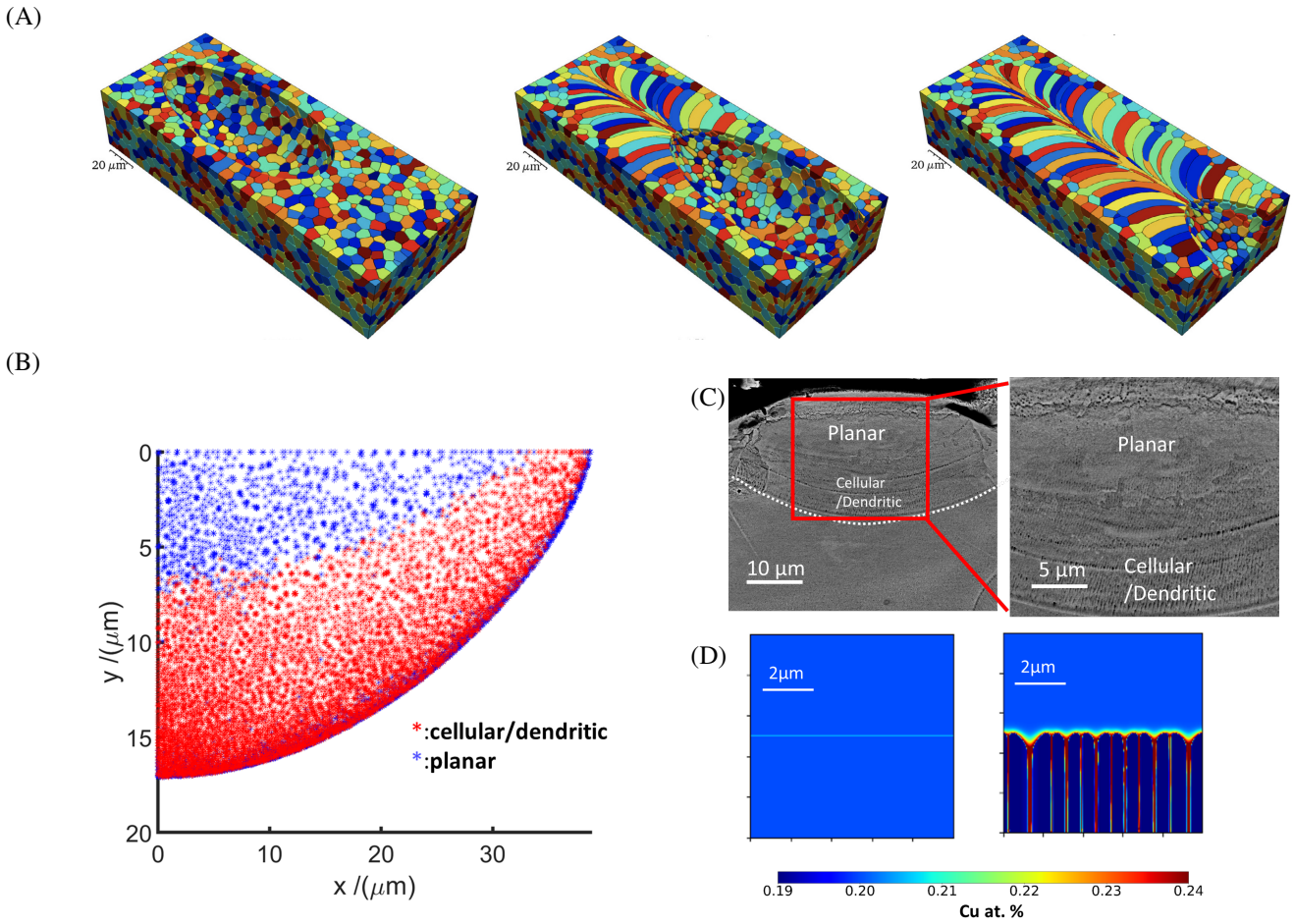

Figure 4: Examples of macro- and micro-structural simulations under AM conditions. ~~(A) Modeling AM ripples as a function of laser power showing ripple occurrence for laser power variation from (a) 300 W, (b) 600 W to (c) 800 W [reproduced from Ref. [87]].~~ (A) Time evolution of the grains along laser progress as calculated using the phase-field method, showing grains melting along the leading edge of the melt pool and formation of grains with higher aspect ratio during cooldown [reproduced from Ref. [88]]. (B, C, and D) Predicted and experimental microstructure distribution for Ni-20 at.% Cu under LPBF (P = 71 W, $|\vec{V}|$ = 300 mm/s, LED = 236.67 J/m). (B) Predicted microstructure distribution. Red symbols indicate the cellular/dendritic microstructural region, while blue symbols indicate planar microstructures. (C) Shows the corresponding experimental counterparts to the simulation. (D) Shows two typical microstructures (i.e. planar (left) and cellular (right)) microstructures predicted using phase-field modeling.

KGT theory can thus be used to predict the microstructure for a given cooling condition by calculating whether a planar or non-planar solidification mode is more stable. These non-planar solidification morphologies include both cellular and dendritic morphologies. Although KGT theory has been used successfully to determine planar/non-planar microstructures from AM processes [91, 92], none of these implementations have been HTP.

In work under preparation, we take the perspective that microstructural design during AM can be achieved by querying the KGT model in an HTP manner. For context the throughput of this implementation is approximately 9 KGT calculations per minute. This can be achieved by using Thermo-Calc's Python API to predict the required inputs for the KGT model from CALPHAD databases. With such a framework, the boundary between cellular/dendritic and planar solidification can be determined for arbitrary alloys. This boundary, which is presented as a function of G and R, can be used to predict cellular/dendritic or planar solidification are likely to occur in a melt pool. The steps in this procedure are as follows: 1) For certain processing parameters, using thermal models, G and R can be predicted at each location in a melt pool, as shown in Figure 5a. 2) Using KGT theory, the boundary between cellular/dendritic solidification and planar solidification can be predicted in 'solidification space' (i.e. G-R space). The Gs and Rs of the melt pool can be plotted over the solidification space and classified as planar or cellular/dendritic, as shown in Figure 5b. 3) These classification results can then be mapped back to the melt pool, as shown in Figure 5c. 4) Finally, this microstructural distribution within the melt pool can be compared to experiments as shown in Figure 5d. Similarly, as detailed in Section 2.1, the area of the cellular/dendritic region in G-R space can be used as an alloy design metric to screen for alloys that have a low tendency to dendritic solidification.

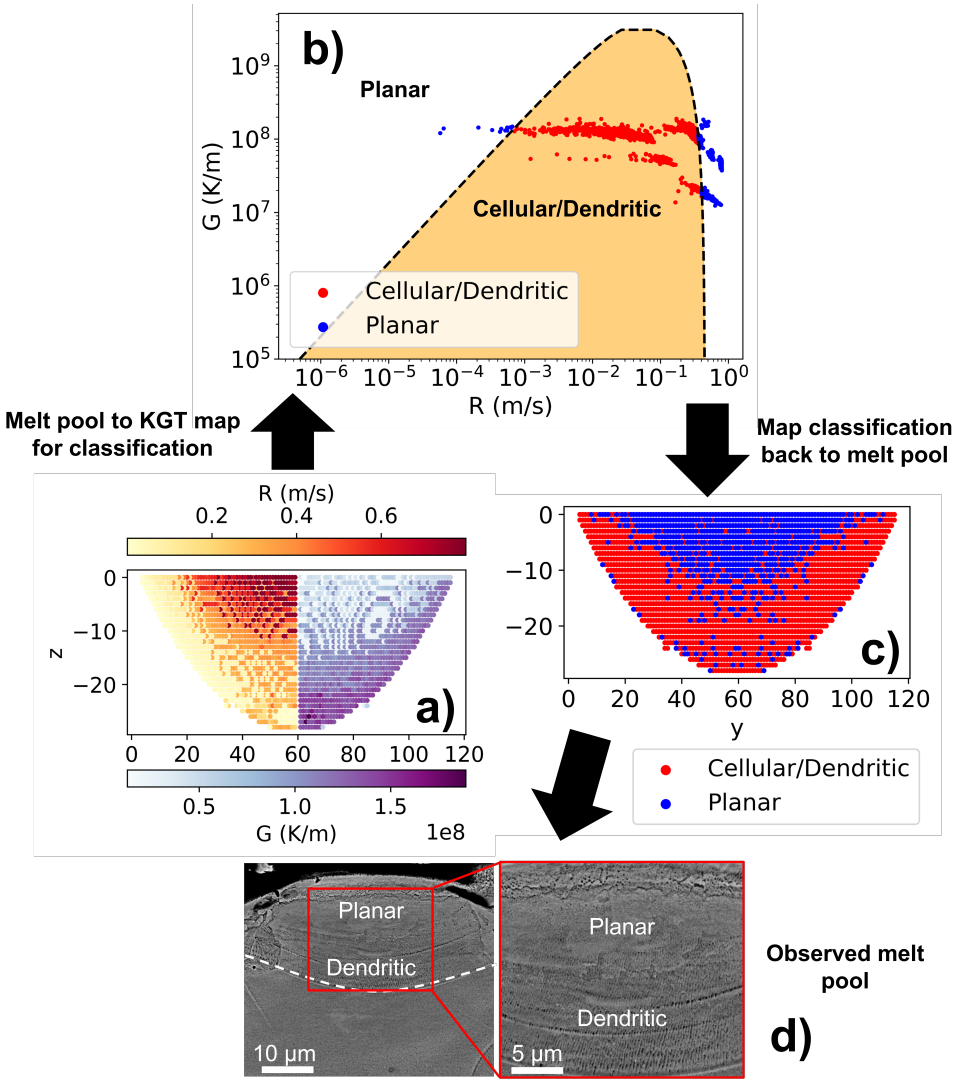

Figure 5: Illustration of the workflow using KGT to predict microstructure selection throughout the surface of the melt pool for a given set of processing parameters.

4. Data Collection and Preprocessing in Additive Manufacturing

The efficacy of computational models, especially machine learning models, hinges on the quality and quantity of their training data. Properly curated and correctly labeled data helps avoid overfitting and diminishes errors. Having a diverse and abundant dataset ensures predictions are not skewed due to noise or biases towards a specific data class. Thus, by leveraging data mining and material informatics, we can enhance computational capabilities, accelerating the transition from alloy design concepts to experimental deployment.

Data mining plays a crucial role in alloy design, as it helps identify correlations, trends, classes, and anomalies within data sets. This process provides valuable insights into the complex interplay between chemistry and physics, allowing for the prediction of material behavior. Notably, Ashby et al. [93] pioneered data mining to investigate material properties and developed maps to visualize the clustering of these properties, laying the foundation for establishing PSPP relationships across different material classes. Using similar data mining techniques in the context of AM can provide insights and patterns that may not have been immediately apparent and help accelerate alloy design for AM [94]. However, to make this a reality, it is necessary to have access to properly curated datasets.

Databases: The initiation of a database is a pivotal step. Taking into account the myriad of variables inherent in AM, it is imperative to have this information organized within a structured framework, ensuring that *apriori* knowledge effectively guides us through the complexities of the AM design space.

Pre-processing and Feature Engineering: To extract valuable information from data stored in databases, pre-processing and feature engineering is a necessity, particularly for ML models. These techniques help eliminate noise and bias, refine the data, and enhance

the model's predictive accuracy.

4.1. Development of AM Databases

The surge in interest in AM in recent years has led to a swift accumulation of experimental AM data. Yet, the AM community still lacks a unified data management framework, leaving most AM data scattered across the literature. Without a centralized data management approach, constructing valuable datasets for ML models becomes challenging. Establishing such a structured system can enhance computational predictions on alloy printability, while also reducing the variance and uncertainties inherent in the AM build process [95].

In other sub-fields of materials science, open-source databases have been developed to organize materials data, enabling its use in ML models or data-driven investigations. For example, open-source databases, such as Materials Project [96] and the Automatic FLOW Frame for Materials Discovery (AFLOW) [97] have enabled a huge amount of ML works in the density functional theory community.

AM databases should prioritize strengthening the PSPP linkages and align with the FAIR Data Principles (Findable, Accessible, Interoperable, and Reusable) [98, 99]. By following the FAIR Data principles, a common framework can be used to aid in establishing a data infrastructure that supports good data management and ensures the reusability of the data. The minimal types of features (see Figure 6) that should be captured in order to make the database maximally useful include chemistry [64, 100], powder morphology [101–103], build information [104, 105], processing parameters [106–108], and properties. By capturing the various variables associated with AM, patterns in data can help to learn the physical phenomena, establish the linkages in the PSPP diagram for AM alloy design, and narrow down the printability space for AM.

Current initiatives, such as the Additive Manufacturing Materials Database (AMMD) by the National Institute of Standards and Technology (NIST) [109] and NASA's AM database [110], aim to create open-source databases for AM. Despite these efforts, comprehensive open-source options are scarce due to the resources required. Many existing databases overlook certain processing parameters or focus narrowly on specific material systems [110, 111]. There is a clear demand for a comprehensive database that can encompass a diverse array of material systems and comprehensively cover each aspect associated with the PSPP framework for AM. The development of such a comprehensive database would pave the way for the creation of data-driven and ML models. These tools would be instrumental in discerning the intricate multivariate relationships between the process parameters, microstructure, and properties of the manufactured products made from scratch, further advancing the understanding and optimization of AM.

4.2. Pre-Processing and Feature Engineering

Upon constructing a database, data sanitization is crucial [112]. This process involves curating data sets by removing outliers and imputing missing values. When dealing with missing data in the context of AM, choosing imputation methods is crucial for the integrity of the analyses and predictions. Traditional single-value imputation methods such as mean, median, mode, or constant imputation are simple but may oversimplify the complexities inherent in AM data. As an example, consider the relationship between laser power and melt pool depth. In AM processes, higher laser power typically correlates with increased melt pool depth. If data on laser power is missing and traditional imputation methods are applied, the correlation between laser power and melt pool depth may be inadequately addressed. This oversight can lead to imputation inaccuracies, impeding a comprehensive understanding of the complex relationships inherent in the AM feature space. A more sophisticated approach benefits AM data, like k-Nearest Neighbors (kNN). The kNN method considers relationships in the feature space and assigns missing values based on the characteristics of nearest neighbors [113]. This is particularly useful in AM, where the relationships between various material properties and processing parameters are crucial in determining the final product's quality.

Multivariate Imputation by Chained Equations (MICE) [114, 115] stands out as a robust method for handling missing data in the context of AM. MICE allows for customized imputation models for each variable. This adaptability proves crucial when dealing with intricate interplays between different aspects of AM. In addition to MICE, advanced model-based imputation methods like random forest imputation [116] and Bayesian regression [117] contribute significantly to handling missing data challenges in AM data sets. Random forest imputation utilizes ensemble learning to provide robust imputations, considering the complexities of AM data. On the other hand, Bayesian regression incorporates probabilistic modeling to capture uncertainties in the imputation process, aligning well with the intricacies of AM data sets.

Hierarchical Gaussian Processes (HGPs) present a non-traditional route in addressing missing data in AM. These methods, known for their ability to model complex dependencies and capture latent structures, offer adaptability across different levels, accommodating variations in the imputation process specific to AM. Refs. [118, 119] demonstrated how HGP regression can combine inexpensive proxy experiments with more costly ones. This approach involves constructing a GP to estimate values for a less expensive proxy experiment across a domain. Subsequently, the estimated proxy experiment values serve as informative features for a GP model

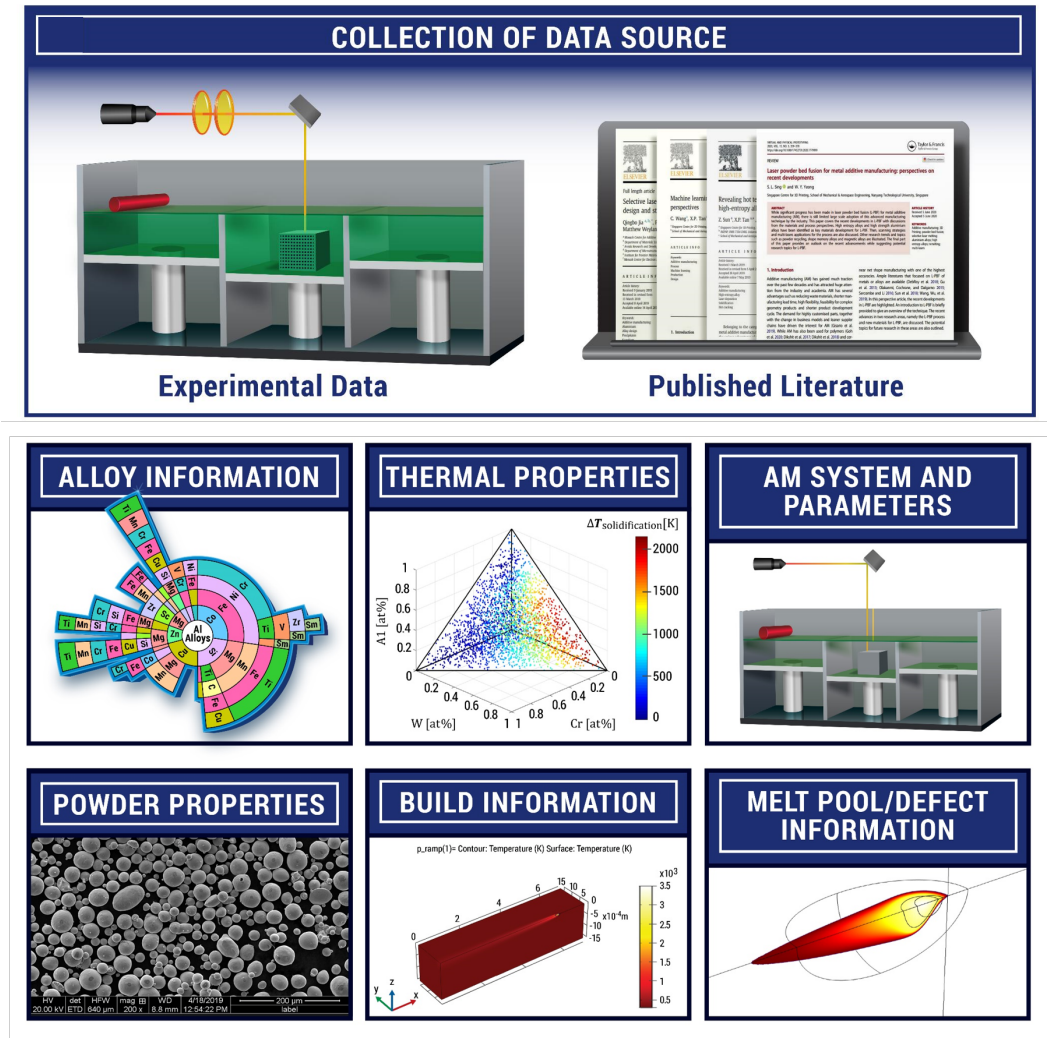

Figure 6: The AM process produces diverse data that can be aggregated into a structured database. Essential features include the alloy's chemistry and thermal properties, machine and processing parameters like laser power, scan speed, and beam diameter, and powder feedstock quality. Factors like substrate preheating and the build process influence defect presence in the final AM product. Accurate measurements of melt pool dimensions and defect labeling are crucial for assessing material printability. By organizing this data, ML models can discern patterns critical for understanding the PSPP relationships in AM.

targeting the more expensive experiment. In Refs. [118, 119], the authors used HGPs to impute hardness values to be used in a yield strength model. By using GPs, underlying correlations between data can be identified and utilized to predict the value for a missing property at a point in the design space.

AM datasets encompass diverse data types, including numerical, categorical, time-series, text, and image data. It is imperative to conduct featurization on each data type. For instance, microstructural images are commonly employed to establish relationships between processes and structures and are generally considered high-dimensional from an ML perspective. Various methods, such as filters [120] and deep convolutional neural networks (CNNs) [121], can be applied to extract features suitable for integration into data-driven and ML models. On the other hand, the categorical data, highlighted by the occurrence of specific defects like keyholing, often require one-hot encoding for optimal implementation in the model.

A data set that effectively mirrors the design space needs sufficient volume and variability. It is also vital to analyze the correlation between features. Various methods can be used to analyze the correlated features. The Pearson Correlation Coefficient [122] offers simplicity in computation and interpretation, proving effective for linear relationships, yet its sensitivity to outliers and assumption of a normal distribution are notable limitations. Spearman Rank Correlation Coefficient (SRCC) [123], a non-parametric approach robust to outliers, is suitable for monotonic relationships but overlooks the magnitude of variable differences. Kendall Tau Rank Correlation [124], also robust to outliers, is beneficial for smaller sample sizes but demands more computational resources. Mutual Information (MI) [125] captures linear and non-linear relationships but is sensitive to variable scale. Liu et al. [126] demonstrated how MI could be utilized in aiding in increasing an ML model's predictive accuracy by aiding in feature selection. A few methods that may need to be avoided due to their limitations and simplicity include Crammer's V and heat maps. Cramer's V measures the association between categorical variables, with the drawback of being confined to categorical data. Heat maps offer visual insights but are limited to visual inspection and may not capture non-linear relationships. The selection of an appropriate method hinges on data characteristics, variable types, and analysis objectives. In addition, exploratory statistical analysis provides immediate insight into data, including examining measures such as mean, median, mode, and standard deviation and assessing data distribution and outliers. Performing these analyses and further pre-processing can enhance a model's predictive accuracy and decrease the computational cost of calculations.

Challenges related to data availability for various material properties may limit a model's predictive accuracy in materials data. In such cases, methods like Crude Estimation of Property (CEP) [127] allows for a rapid assessment of a property for many materials while conserving computational resources. During CEP, the target property is estimated with a fast-acting, low-fidelity model. This low-fidelity prediction is then used as an informative feature in an ML model. CEP is a pragmatic solution for data augmentation and initial screening, providing quick and rough estimates of material properties. Its computational efficiency is particularly evident in resource-constrained scenarios.

Featurization extracts crucial information from datasets, highlighting potential correlations among features or between features and specific outcomes like alloy printability or as-built part conditions. This process can refine or combine features to improve model accuracy. For example, Wang et al. [112] introduced composition-based feature vectors CBFV) capable of transforming compositions of an alloy as descriptive inputs for a model. The CBFVs are a data-driven method that contains descriptive statistics about the constituent elements and allows for interpretable information about the alloy system.

In metal AM, the high dimensionality of data poses challenges in discerning trends. Addressing this complexity requires techniques to simplify the data. Principal Component Analysis (PCA) is a widely used method for reducing the dimensionality of data by constructing principal components. This process ensures that the variance of the original feature space is preserved. [128]. Although PCA can simplify complex data, it is essential to acknowledge its limitations. While PCA may reduce data complexity, the amalgamation of potentially relevant features into principal components can obscure scientific insights. To address this, we propose that PCA be complemented with interpretability-focused methods or utilized primarily for initial data exploration. Techniques such as t-distributed Stochastic Neighbor Embedding (t-SNE) [129, 130], domain-specific interpretation strategies [131, 132] and post-PCA feature importance analysis [133, 134] are suggested to supplement PCA. Emphasizing considerations beyond linear feature relationships, non-linear dimensionality reduction techniques like t-SNE and Uniform Manifold Approximation and Projection (UMAPs) [135] can address PCA's inherent limitations of linearity. In addition to mapping non-linear relationships, these methods can help visualize the design space for materials discovery[130, 136–138]. By closely examining the loadings and their absolute values, feature importance analysis offers a potential means to identify influential variables within the transformed feature [139–142]. This process provides insights into the significance of each feature, potentially contributing to an improved understanding of the principal components and original features. As a result, this approach, coupled with visualization, can enhance the overall interpretability of PCA results, addressing the challenges posed by its inherent lack of interpretability.

The engagement of domain experts in the interpretation process is advocated to deepen understanding within the specific alloy design context for AM. Techniques such as biplot analysis [143] and sparse PCA [144] are suggested as additional tools for improving interpretability. Biplot analysis visually represents the observations and variables in a two-dimensional space, allowing for the simultaneous examination of their relationships. It aids in identifying patterns, trends, and the contribution of each variable to the principal

components. Wong et al. [143] used PCA for dimensionality reduction in the relationship between the quality of a build and AM process parameters. Specifically, PCA is employed to reduce the dimensionality of all process parameters into two variables (PC1 and PC2) for visualization, allowing a comparison between volume energy density and PCA in capturing the correlation between process parameters and material properties. The biplot representation displays the transformed space, where the length of arrows indicates the strength of individual process parameters with respect to their PC direction, and the angle represents their contribution to a PC. The biplot analysis reveals that layer thickness and hatch spacing contribute mostly to PC1, while laser speed primarily contributes to PC2. Laser power shows a significant correlation with all other studied process parameters. The angle and length of the arrows suggest influential variables for constructing PC1 (layer thickness, hatch spacing, and laser power) and PC2 (laser speed). On the other hand, sparse PCA introduces sparsity constraints during the analysis, emphasizing a subset of features that significantly influence each principal component. By promoting a focused and selective representation, sparse PCA enhances the understanding of the key variables contributing to the variance captured by the principal components. Integrating these techniques with PCA offers a more comprehensive and nuanced interpretation of the underlying relationships in the context of alloy design for AM.

Proposing integration with methods like Shapley Additive Explanations (SHAP) [145] alongside PCA further enhances interpretability, leveraging SHAP values to bridge the gap between PCA-transformed data and model predictions. In the context of AM data, SHAP values can comprehensively understand how each feature influences the data. They reveal the contribution of each input variable to the model's prediction. This is exemplified by Zadeh et al. [117], who utilized SHAP to explore the interpretability of predictions related to the transformation temperatures of shape memory alloys.

A comparable technique to SHAP, which enhances the interpretability of ML models, is Local Interpretable Model-agnostic Explanations (LIME) [146]. LIME offers a more localized explanation of how the input features influence each individual prediction. This capability makes LIME a powerful tool for troubleshooting and refining AM processes by identifying factors that lead to suboptimal outcomes. Integrating techniques such as SHAP and LIME, with or without Principal Component Analysis (PCA), can lead to interpretable AM models. By combining these methods, researchers and engineers can gain global and localized insights, fostering a clearer understanding of the relationships within the data. This, in turn, facilitates more informed decision-making in alloy design and process optimization, ultimately contributing to advancements in AM.

Feature engineering is a pivotal component in ML. Various methods can be used to feature raw data to improve model performance and interpretability. A few common techniques used for data sets, including AM data sets, are normalization and feature scaling. Normalizing and scaling the features ensures that different features contribute proportionally to the model, preventing one feature from dominating others due to differences in scale. Such scaling is in line with best practices for ML [112]. For example, Liu et al. [147] used a GP regression model to establish a relationship between the process parameters and the relative density of AlSi10Mg parts fabricated using L-PBF. The inputs were normalized to be non-dimensional, and the relative density was normalized to have a zero mean. The model exhibited a high accuracy with a prediction error of less than 0.3%. Apart from normalizing and scaling features, alternative techniques like one-hot encoding [148] for handling categorical features, and the use of CBFVs [112], as previously discussed in this section, can be employed for featurizing AM datasets.

Futhermore, Automatic Feature Engineering (AFE) can be used to extract meaningful insights for interpretable predictions in ML tasks. AFE proves particularly advantageous within materials science applications. Notably, AFE can generate interpretable functional formulas, shedding light on the physics underlying materials systems and guiding the discovery of new materials. Xiang et al. [149] developed a strategy that employed feature generation trees (FGT) in conjunction with deep Q-networks (DQN) to efficiently explore the expansive feature space, facilitating the scalable extraction of predictive features. This method allows for the generation of interpretable functional formulas, highlights the physics underlying the material system, and guides the discovery of new materials. In the context of AM data sets, leveraging FGT with DQN stands out as a promising avenue for enhancing feature engineering methods. The dynamic exploration of the intricate feature space associated with AM, facilitated by FGT with DQN, holds the potential to extract relevant features crucial for predicting and optimizing material performance. This innovative approach, combining FGT and DQN, could enhance model interpretability and provide a systematic way to discover novel materials tailored to the specific requirements of the AM process. The insights from interpretable functional formulas may pave the way for more informed decision-making in alloy design and material discovery within the additive manufacturing landscape.

Symbolic regression, another potent feature engineering method, involves discovering mathematical expressions representing data relationships. Mojumder et al. [150] used a neural network-based symbolic regression to help establish the relationship between the process parameters and LOF porosity for Ti-6Al-4V and other materials. The authors obtained mechanistic expressions that successfully captured the relationship between the process parameters and LOF. Tools like Eureqa [151, 152] and AI Feynman [153] facilitate symbolic regression tasks. Lee et al. [154] utilized Eureqa to identify a symbolic regression expression that helped establish a relationship between the scan track width and process parameters to print single tracks and multilayer thin-walled structures. Integrating symbolic regression with other techniques broadens the feature engineering landscape in AM models, enabling a comprehensive understanding of underlying dynamics for improved predictions. However, such techniques can be computationally expensive as the complexity of the expressions increases. In addition, this method may compromise the interpretability of the model for high-dimensional data sets.

Shen et al. [155] introduced Clustered Discriminant Regression (CDR) as a potential method for addressing high-dimensional data sets. This method employs a clustering approach to group features and performs feature extraction within each cluster. The primary goal of CDR is to conduct feature selection while minimizing error. Demonstrating its effectiveness, CDR outperformed CNN in classifying AM images. However, it is essential to note that CDR may incur computational expenses due to its greedy nature.

For high-dimensional data sets, an alternative approach is the Sure Independence Screening and Sparsifying Operator (SISSO), which addresses challenges associated with such data sets through a two-step process [156]. The Sure Independence Screening (SIS) step involves ranking features based on their correlation with the target variable, ensuring the retention of informative variables. The subsequent sparsifying operator refines the selected features by capturing non-linear relationships and interactions, proving advantageous in scenarios with data sets containing numerous features. SISSO has demonstrated success in materials science where Singh et al. [157] used SISSO to aid in assessing the impact of chemical alloying on the formation enthalpy of rare-earth intermetallics. SISSO incorporated meaningful atomic features and accurately predicted the formation enthalpies of rare-earth compounds. The model was applied to explore the impact of transition metal alloying on the energy stability of Ce-based cubic Laves phases. The predictions aligned well with DFT calculations and X-ray diffraction measurements, offering guidance for compositional considerations in ML and the discovery of new metastable materials. The electronic structure of a specific compound was analyzed to deepen the understanding of phase stability. This integrated approach provides a fast and reliable design guide for discovering technologically valuable materials. In AM, where understanding the relationships between process parameters, material properties, and print quality is paramount, SISSO can contribute by efficiently handling the complexity of the feature space. By incorporating SISSO into the analysis of AM data sets, the potential key relationships can be uncovered, process parameters can be optimized, and the overall quality of additive manufacturing can be enhanced.

In addition to these techniques, feature selection methods further enrich the feature engineering landscape. Summers et al. [158] applied Recursive Feature Elimination with cross-validation (RFECV) to develop process maps that link various process parameters in pulsed wave laser AM. Comparing the performance of the selected features to those chosen using alternative methods emphasizes the effectiveness of RFECV in enabling the creation of interpretable process maps. This approach, initially applied to pulsed wave laser AM, may also prove applicable to L-PBF. Moreover, clustering methods, such as hierarchical clustering, offer another avenue for feature selection. Yao et al. [159] integrated hierarchical clustering with a support vector machine classifier to systematically identify and recommend AM design features for a target objective. However, it is crucial to note that RFECV and hierarchical clustering are greedy approaches. While effective in feature selection, these methods may incur substantial computational costs. Therefore, careful consideration of computational resources is essential when implementing these approaches for feature selection in the context of metal AM datasets. This comprehensive approach, encompassing traditional feature engineering techniques and advanced feature selection methods, ensures a nuanced exploration of the feature space in metal AM datasets, ultimately improving model interpretability and predictive accuracy.

5. Overview of Machine Learning and Data-Driven Approaches

5.1. Deep Learning for Additive Manufacturing

ML has become pivotal in various modern domains, influencing materials science in a prominent way, especially in AM. It is actively reshaping methods for optimizing material composition and the design of complex structures. In the realm of materials science, ML facilitates image interpretation of microstructures, translates experimental results into actionable insights, and customizes material attributes according to specific design needs. A notable subset of ML is deep learning [160], crucial to deciphering intricate relationships in material data, thus catalyzing breakthroughs in the materials sector [161–163].

The term 'deep' in deep learning refers to the utilization of deep neural networks (DNN), constructed of multiple layers of interconnected nodes, also known as neurons. These networks learn to represent data proficiently through layered learning. They have achieved tremendous success across various applications, marking significant progress in fields like image analysis, text enhancement, voice recognition, autonomous vehicles, and healthcare, to name a few. Widely recognized deep learning structures encompass CNNs for image-related tasks and recurrent neural networks (RNNs) for sequential data, with more modern introductions like transformers and generative adversarial networks (GANs). The role of ML in AM is typically categorized into design, process, and production aspects [112].

Deep learning in AM design: In the context of AM, deep learning offers numerous benefits and advancements, including design, process / build interactions, quality analysis *in − situ* and/or in real-time, and distortion prediction, among others. Recent progress in ML empowers the transition from merely predicting material properties to actively designing alloys in the context of chemistry and microstructure-sensitive design [40, 164, 165]. Tanga et al. [166], for example, have studied the interrelationship between alloy composition, processability, and mechanical behavior in AM Ni-based superalloys, resulting in two new printable alloys in this chemical space. The new alloys demonstrate superior processability and mechanical behavior. Recently, Despress et al. [167] have

trained an asymmetric autoencoder capable of both analysis and synthesis of AM-based micro-lattices where the autoencoder learns the mapping from structure to physical properties and the decoder learns the mapping from physical properties to structure. Kim et al. [168] trained a DNN capable of making reliable predictions for a forward design approach, enabling an efficient search for superior materials far beyond the domain of the initial training set. Yazdi et al. [169] proposed a hybrid DNN structure with two types of input data to monitor the process parameters that result in porosity defects in printed cylindrical layers. Furthermore, deep learning has been used to aid in developing predictive models that optimize material composition and printing parameters, leading to enhanced material properties and performance.

Deep learning in AM process control: Deep learning algorithms have also been used to analyze complex data patterns, allowing the identification of defects and anomalies in the AM process [169–171]. This allows real-time process monitoring and control. Shevchik et al. [172] presented a framework for real-time quality monitoring based on spectral CNN trained with acoustic emission data. Yang et al. [173] developed a deep learning-based melt pool classification method to quickly and accurately analyze (and potentially control) the size of the melt pool in L-PBF AM. An overview of quality analysis in metal AM using deep learning is given in [174]. In essence, extracting insights from multi-modal sensory data is crucial for addressing challenges in AI-assisted manufacturing, including detecting visual defects; however, the industry needs standardized processes and aligned methodologies in order for this technology to be widely adopted. Ahuja et al. [175] discussed some of these key challenges for AM to become a mainstream production technology, and deep learning tools are likely to greatly assist in this transition.

5.2. Deep learning of AM process maps

As discussed in Section 2.2, printability maps in AM serve as a graphical representation that connects the process conditions to printing outcomes [16]. Printability maps in AM guide users in optimizing parameters to ensure high-quality prints while reducing defects such as balling, cracking, and porosity, addressing key challenges in AM [176]. The concept of printability maps emerges from the recognition that multiple factors—such as process parameters, materials properties, and local geometry/topology —influence the success of a 3D print. Factors commonly featured in printability maps include layer thickness, printing speed, substrate temperature, etc.

Printability maps can be derived from experiments, simulations, or both. Johnson et al.[16] suggested a simulation-based prediction method for predicting the printability of an alloy printed under L-PBF conditions. In their framework, the formation of defects was connected to melt-pool geometry, and the latter was calculated with a high-fidelity FEM or a low-cost Eagar-Tsai (E-T) model [37]. Sheikh et al. [80] developed a physics-based framework using NN emulators of the ET model to predict melt pool geometry in a HTP manner. This emulator approach was orders of magnitude more efficient and enabled for a very rapid assessment of the printability map of alloys of arbitrary composition. In that work, a new 'printability index' was defined as the fraction of a standard L-PBF space free from porosity defects. Figure 7a displays printability maps for five alloys with printability indices ranging from 25.6% to 31.9%. Both values surpass the printability index of 22.2% index for equiatomic CoCrFeMnNi. This printability index could be used as an optimizable feature in future efforts to design alloys specifically for AM.

On the other hand, a major challenge is to understand the deep connections between process parameters, material properties, and printability. Recently, we have used a Variational AutoEncoder (VAE) model (Fig. 7b) to discover such connections. The predicted printability maps of different alloys, along with their chemistry and AM-relevant thermophysical properties, were fed to the encoder network to 'learn' the latent space connecting the printing results to alloy chemistry and material properties, as shown in Fig. 7c. The decoder network was, in turn, used to reproduce new printability maps from this latent space for novel alloy chemistry. With sufficient training data, this VAE model would be capable of generating plausible printability maps for new alloys at a much lower cost compared to other approaches.

5.3. Bayesian and/or Closed-Loop Approaches

In Section 2.1, we showcased the exploration of the chemistry-process space through HTP methods using straightforward indicators. However, with the requirement for AM thermal simulations and single-track experiments to validate an alloy's printability, a HTP factorial assessment of the design space becomes prohibitively costly. A major limitation of traditional ICME approaches is their tendency to be 'one-shot' or 'open-loop.' Essentially, although powerful, these approaches do not allow for a strategic and efficient allocation of resources based on insights gathered from simulations and experiments [32]. In contrast, Bayesian methods provide a rigorous framework to update prior knowledge when new useful information becomes available. Thus, they excel in this scenario by optimally allocating resources based on prior insights, data from simulations, and findings from experimental campaigns.

Bayesian methods have gained traction in AM, particularly for calibrating intricate simulations. As an illustration, Ye et al. [177] used Bayesian networks (BN) to fine-tune a set of interconnected models, notably a FEM-based thermal model followed by a phase field model. The inputs, outputs, and hyperparameters of both models are represented as the BN shown in Figure 8. Note that,

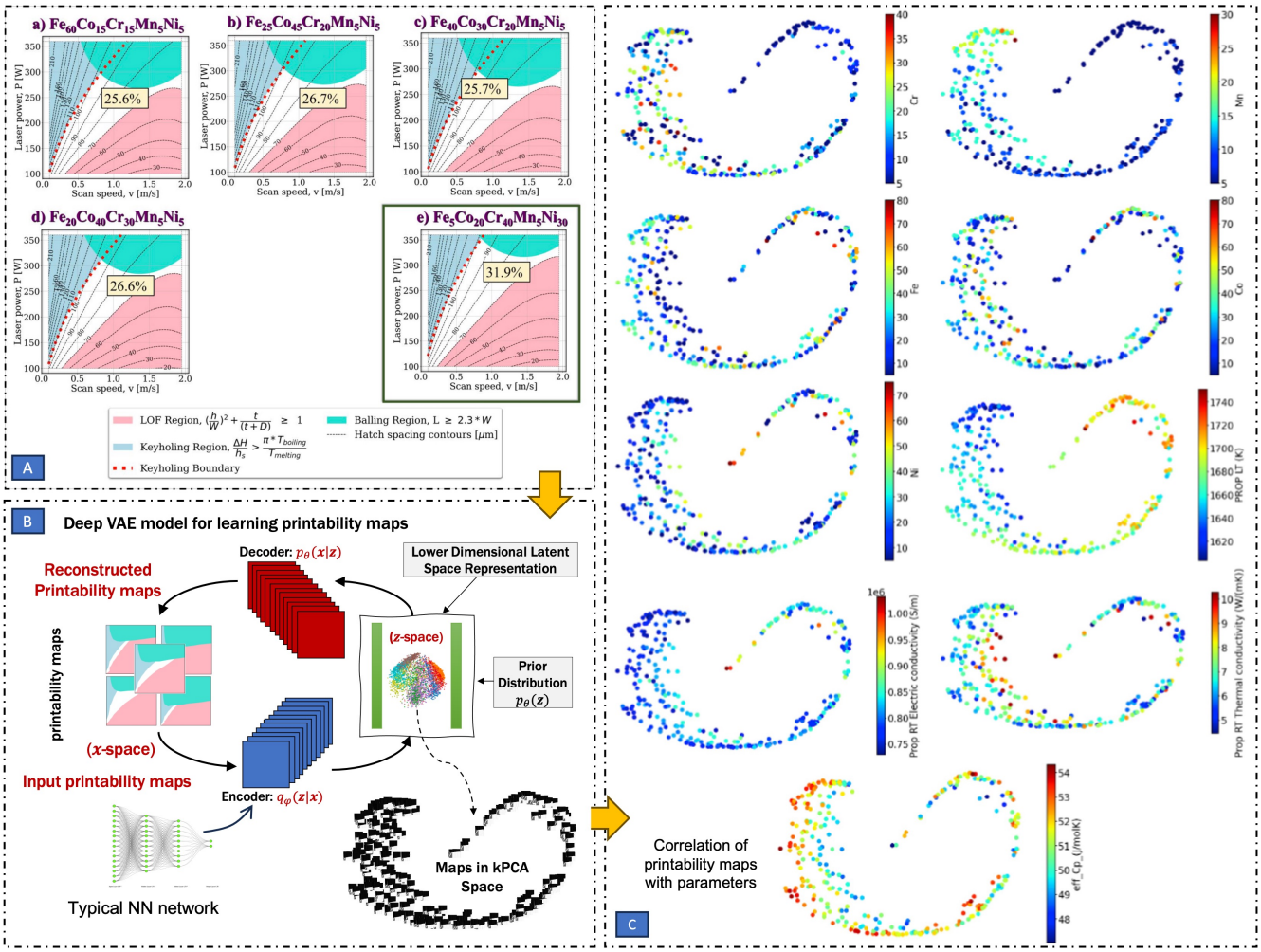

Figure 7: A) Printability maps with the optimal combination criteria set for the five alloys were fabricated using the dimensionless E-T model [Reproduced from Ref. [80]]. The maximum printability index obtained was 31.9% for $Fe_5Co_{20}Cr_{40}Mn_5Ni_{30}$ and the minimum value for the printability index was 25.6%. The values are greater than the printability index for the printability maps for the equiatomic CoCrFeMnNi using the dimensionless E-T model of 22.2%. B) Typical architecture of a deep variational auto-encoder involving neural networks in the encoder and decoder part and a latent space where the provided printability maps can be rearranged to establish correlations with alloy chemistry [Reproduced from Ref. [40]]. C) Some of the established connections in the latent space of VAE model, i.e., each point corresponds to a printability map in kernel PCA (kPCA) space and the figures show how the alloy chemistry or properties change.

in this BN setting, the output of the FEM-based thermal model is the input to the PFM. Given the structure of the BN and a set of experimental data (melt pool width for the thermal model and primary dendritie arm (PDA) spacing for the PFM), the authors calibrated the parameters of both models at the system level.

Beyond BN, there are other Bayesian approaches to model calibration that can be quite useful in the context of AM co-design. For example, the work by Mahmoudi et al. [178] is Bayesian in two ways: 1) using a non-parametric, Bayesian approach to regression (i.e. a Gaussian Process Regressor (GPR)) the authors create a faithful emulator for expensive FEM-based single-track AM simulations. 2) Using this fast-acting thermal model emulator, the authors perform Bayesian Monte Carlo-based calibration to tune three unknown material parameters (powder bed porosity, laser absorptivity, and coefficient of thermal conductivity for liquid). Zhang et al. [26] expanded this technique and applied it to calibrate printability maps (see Section 2.2). In that work, an emulator was created for a thermal model (the analytical ET thermal model instead of a FEM-based model as in Ref. [178]). Three material parameters required by the ET model were then calibrated using the Bayesian Monte Carlo-based calibration method. This essentially creates a 'corrected ET model' whose predictions are used to generate a corrected printability map (see Section 2.2 for details on printability maps). The closed-loop Bayesian nature of the calibration scheme is shown in Figure 8.

Bayesian *optimization* offers an alternative to calibrating models, compared to previous methods that rely heavily on resource-intensive Monte Carlo techniques to discern the posterior distribution of hyperparameters. As a case in point, Ghumman et al. [179] utilized Bayesian optimization (BO) to refine the parameters of a cellular automaton microstructure model [180], designed to predict microstructures after AM processing. In essence, BO aimed to minimize a metric—the angularly-resolved chord length distribution [181]—which gauges the visual disparity between observed experimental microstructures and their simulated counterparts. Remark-

ably, the simulations reached satisfactory accuracy after only seven evaluations of the ground truth. Such microstructural considerations are important, as grain morphology has a direct impact on mechanical properties and the tendency toward hot cracking, as further discussed in Section 3.

The works above deal with the calibration of models, which is a vital aspect of AM research. However, there is a noticeable lack of studies on the application of Bayesian approaches for the *design*and *optimization* of alloys and the processing parameters required to print them. That is to say, no closed-loop BO strategies have been deployed to customize metallic materials for both performance and suitability for 3D printing as per the authors' knowledge. The closest instance of an AM Bayesian optimization scheme is that of Deneault et al. [182], which focused on polymer printing. Regardless, in their work, the authors coupled an autonomous AM research robot that is capable of analyzing the results of its own experiments using a BO scheme to tune processing parameters in an automated way. Such works are in line with recent initiatives for autonomous materials discovery [183–185]. This marked a pioneering step in the domain, albeit in a nonmetallic context. BO has been successful in a wide variety of materials science domains, such as metallic film design [186, 187], chemical design [188–190], and alloy design [137, 191, 192]. This indicates that BO can potentially be extended to alloy-process co-optimization.

In Figure 8, we see a representation of the closed-loop BO scheme, a method particularly tailored for the challenges presented by AM. The real power of this approach lies in its ability to efficiently navigate the expansive design space inherent in AM. This attribute drastically reduces the need for exhaustive tests or simulations, an important advantage when considering a problem as complex as the concurrent exploration of vast chemical and processing spaces. Moreover, this scheme is proficient at assimilating both epistemic and aleatory uncertainties. Such a seamless integration ensures a robust and systematic exploration of the AM design space, even in the face of imprecise measurements, be it melt pool dimensions or fluctuating crack densities. However, the hallmark of the closed-loop BO scheme is its ability to learn iteratively. As the algorithm progresses, it refines its recommendations based on feedback from previous experiments, setting the stage for increasingly informed and nuanced decisions.

Figure 8 offers a perspective on potential BO campaigns applied to AM that are conspicuously lacking in the current literature. In this hypothetical scenario, the objective is to design a high-strength, printable alloy. Single-track experiments might serve as the pivotal information source for evaluating the suitability of a given chemistry-process combination. Specifically, the length, width, and depth of the melt pool can be optimized so that the optimal melt pool is hemispherical with a specified radius. A hemispherical melt pool is likely to avoid keyhole and balling defects since these defects are geometrically defined by large W/D and L/W aspect ratios, respectively. LOF can be avoided by ensuring that the radius of the hemispherical melt pool is sufficiently large such that the melt pool fuses with the underlying layers (see Section 2.2 for more details).

Once a single-track experiment has been performed and acceptable results are achieved, a cube of material can be printed and tested for Vickers hardness (HV) testing. HV acts as a convenient proxy for yield strength (through the Tabor relation [119]), offering a more efficient alternative to tensile tests typically used to measure yield strength. As data establishing the printability and hardness of a particular alloy-process pair accumulate, it becomes the basis for a Gaussian Process Regression (GPR) surrogate model, which will be used to predict the hardness and printability of the remaining untested designs. The prediction and uncertainty in the GPR predictions are then fed to an acquisition function, which uses statistical principles to recommend the most beneficial experiment to conduct next. Once this experiment is performed, the new data are then used to refine the GPR surrogate model, and this closed-loop repeats until the framework has converged on an acceptable design (i.e. an alloy-process pair that results in a circular melt pool and whose resultant printed material has an optimally high HV).

Once a single-track experiment has been performed and acceptable results are achieved, a cube of material can be printed and tested for Vickers hardness (HV) testing. HV acts as a convenient proxy for yield strength (through the Tabor relation [119]), offering a more efficient alternative to tensile tests typically used to measure yield strength. As data establishing the printability and hardness of a particular alloy-process pair accumulate, it becomes the basis for a surrogate model, which will be used to predict the hardness and printability of the remaining untested designs.

There are many choices of surrogate models for BO. For example, deep learning models, such as those mentioned in Section 5.1 are an attractive option when data is abundant. However in practice AM datasets are often sparse (see Section 4.1), and thus such data-hungry methods may not be suitable. A more common choise of surrogate model for BO is the Gaussian Process Regressor (GPR). GPRs are often used for BO due to a few key characteristics:

- GPRs exploit the fact that the data being modeled is not random, but instead accounts for correlations between training data [193]. The kernel function determines the shape and strength of these correlations [193]. Furthermore, this kernel can be engineered (an active field of research itself [194–196]). Prior physics-based knowledge about the property of interest can be embedded in the kernel which can ease data-burdens on the GPR [194], effectively combining experimental data with a prior hypothesis about the shape of the underlying ground-truth.
- Another method of imbuing physics into GPRs is via the prior mean function [119]. Recall that GPRs are Bayesian models,

meaning they rely on a prior prediction which is updated in light of observations [193]. In the case of GPRs, this prior prediction is the prior mean function [193]. When predicting in regions in the domain where data is present, the GPR will output values similar to training data, however when predicting in regions of the domain where data is sparse, the GPR start defaulting to its prior, i.e. the prior mean function. Typically this prior mean function is set to 0, however often overlooks the fact there are often first-approximation models that can orient the BO scheme with global trends [119]. It is our perspective that agumented the prior mean function of GPRs with physics-based prior knowledge is crucial to performing BO in the vast union of chemistry and processing spaces.

The prediction and uncertainty from the surrogate model are then fed to an acquisition function, which uses statistical principles to recommend the most beneficial experiment to conduct next. Once this experiment is performed, the new data are then used to refine the GPR surrogate model, and this closed-loop repeats until the framework has converged on an acceptable design (i.e. an alloy-process pair that results in a circular melt pool and whose resultant printed material has an optimally high HV).

Although this was just a *prospective* of what potential closed-loop AM campaigns might look like, it is our *perspective* that there exists a great opportunity to use BO to recommend an optimal design of AM experiments to quickly identify and optimize useful *and* printable alloys.

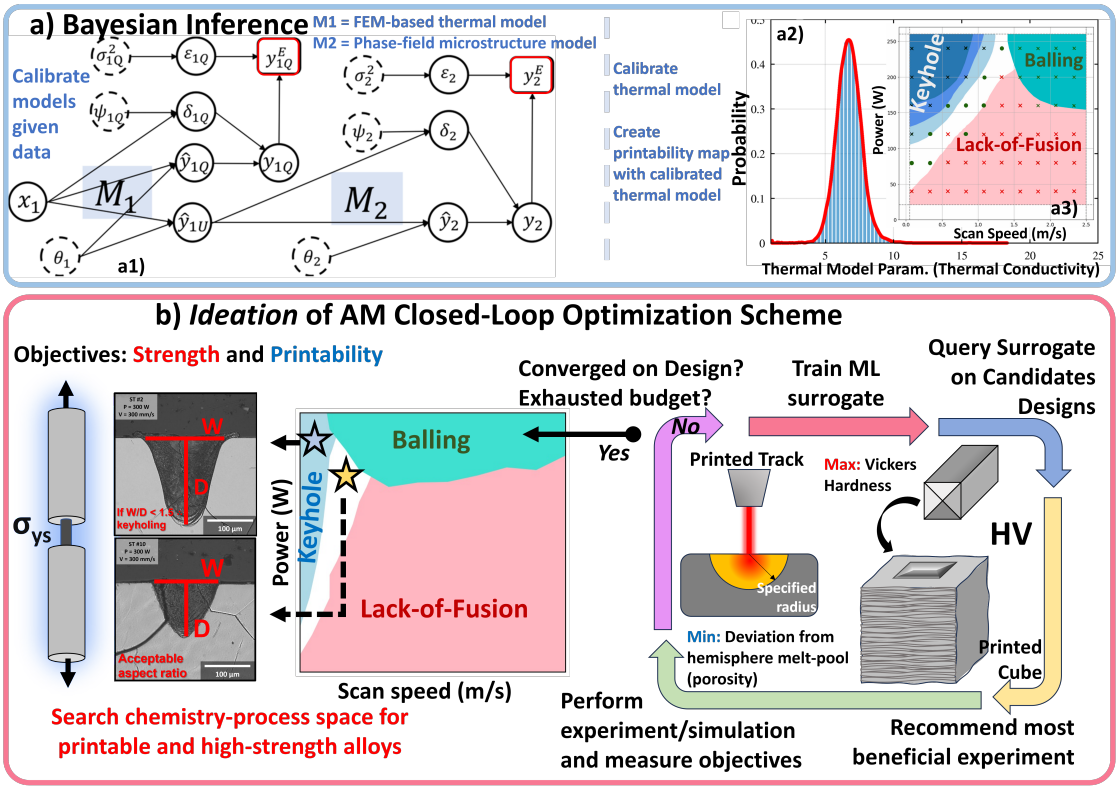

Figure 8: a) Various works where Bayesian inference was used in the context of AM. a1) A BN used to calibrate two coupled models at the system level [Reproduced from Ref. [177]]. a2) Posterior distribution of the thermal conductivity after Bayesian calibration [Reproduced from Ref. [178]]. a3) Data-corrected printability map from Bayesian calibration [Reproduced from Ref. [26]]. b) Hypothetical BO campaign where the objective is to design a high-strength, printable alloy. Specifically, the melt pool geometry is to be optimized such that it is hemispherical with a specified radius, thus avoiding lack-of-fusion, keyholing, and balling. Once satisfactory sinlge-track results are obtained, a cube of material can be printed and tested for Vickers hardness (HV) testing.

6. Conclusion

Developing alloys tailored for L-PBF presents significant challenges because of the high cost of AM experiments and the extensive array of alloys and L-PBF process parameters to consider. The interaction between alloy compositions and processing parameters can lead to numerous printability challenges, including issues such as porosity and cracks. As a result, the design process for AM can be characterized as a complex multi-objective optimization problem, marked by substantial variability in both macro- and microstructural features. These variations are a direct result of the intricate thermal histories experienced during the printing process, which significantly impact the product's performance. Therefore, relying solely on experimental approaches is not feasible for designing within the chemistry and L-PBF process parameter design spaces.

In this study, we provided a perspective on the use of ICME and data-driven tools to establish PSPP relationships in the context of metal AM. By leveraging these tools, we propose that a co-design approach can be deployed to develop alloys that *simultaneously* meet application-driven performance requirements and are printable. Based on the available literature and our experience with HTP alloy design, it is our perspective that the ideal AM design campaign is as follows.

- In AM alloy design, an early assessment of the chemistry-processing space is crucial to exclude alloy-process pairs susceptible to defect formation. In Section 2.1, we showed how using $fast-acting$, physics-based printability indicators offers an efficient way to navigate the chemistry-process space, targeting alloy-process combinations likely to produce defect-free prints.
- After refining the design space, we can focus on analyzing the top alloy-process pairings. In Section 2.2, we showed how physics-based thermal models simulate melt pool geometry. From this geometry, printability maps can be derived.
- After the computational assessment of alloy printability and the identification of a subset of alloys with promising printability, the focus can be shifted toward the printed microstructure. In Section 3, we discussed how the analytical KGT model, when implemented in an HTP context, can be used to investigate the microstructure selection problem across vast chemical spaces. These inexpensive predictions can then be cross-validated against higher fidelity PFMs as well as experiments.
- After identifying alloy-process combinations likely to yield prints free of cracks and porosity with the desired microstructures, the next step involves experimental testing. Such experimental results can be combined with data from the existing literature and curated into databases. Section 4 delves into best practices for database creation, specifically tailored to the AM context.
- Using curated datasets from AM experiments, one can employ data-driven models for both experimental modeling and design. In Section 5.1, we highlight how deep learning facilitates the recognition of complex patterns and correlations among various materials and process parameters. Similarly, Section 5.3 illustrates the application of Bayesian methods for multi-source information modeling and orchestrating closed-loop experimental campaigns.

In conclusion, this study has provided a perspective on computational tools and their pivotal role in advancing alloy design for AM, with a particular emphasis on establishing the PSPP relationships in AM alloy design. Through the utilization of these tools, we advocate for a co-design methodology that harmonizes printability- and performance-driven materials design. Despite the challenges that remain, the combined use of computational tools and experimental data holds the potential to unlock the full capabilities of AM co-design. We point out that the proposed framework will not replace experiments, as they are the ultimate arbiters of what is truly possible and feasible. However, a computational approach is necessary to accelerate the design-to-deployment cycle.

Acknowledgements

Support from the Army Research Office (ARO) under Contract No. W911NF-18-1-0278 is acknowledged. BV and SS acknowledge Grant no. NSF-DGE-1545403 (NSF-NRT: Data-Enabled Discovery and Design of Energy Materials, D^3EM). BV acknowledges the support of NSF through Grant No. 1746932. VA acknowldges the support from Texas A&M Institute of Data Science (TAMIDS). RA, AE and IK acknowledge support from NSF through Grant No. DMREF-2323611. The authors also acknowledge the NASA-ESI Program under Grant Number 80NSSC21K0223. High-throughput CALPHAD calculations were carried out in part at the Texas A&M High-Performance Research Computing (HPRC) Facility.

Declaration of generative AI and AI-assisted technologies in the writing process

During the preparation of this work, the author(s) used ChatGPT version 3.5 in order to ideate/brainstorm alternative sentence structures and stylistic choices in limited sections of the paper. Generative AI was used on a sentence-by-sentence basis and was not used to generate complex sentence structures. After using this tool/service, the author reviewed and edited the content as needed and take full responsibility for the content of the publication.

Declaration of Interest

The authors declare that they have no known competing financial interests or personal relationships that could have appeared to influence the work reported in this paper.

References

[1] D. Thomas, Costs, benefits, and adoption of additive manufacturing: a supply chain perspective, The International Journal of Advanced Manufacturing Technology 85 (2016) 1857–1876.

[2] M. Korpela, N. Riikonen, H. Piili, A. Salminen, O. Nyrhilä, et al., Additive manufacturing—past, present, and the future, Technical, economic and societal effects of manufacturing 4 (2020) 17–41.

[3] A. Bandyopadhyay, K. D. Traxel, M. Lang, M. Juhasz, N. Eliaz, S. Bose, Alloy design via additive manufacturing: Advantages, challenges, applications and perspectives, Materials Today 52 (2022) 207–224. doi:https://doi.org/10.1016/j.mattod.2021.11.026.
URL https://www.sciencedirect.com/science/article/pii/S1369702121004314

[4] D.-G. Ahn, Directed energy deposition (ded) process: State of the art, International Journal of Precision Engineering and Manufacturing-Green Technology 8 (2021) 703–742.

[5] M. Schmidt, M. Merklein, D. Bourell, D. Dimitrov, T. Hausotte, K. Wegener, L. Overmeyer, F. Vollertsen, G. N. Levy, Laser based additive manufacturing in industry and academia, CIRP Annals 66 (2) (2017) 561–583. doi:https://doi.org/10.1016/j.cirp.2017.05.011.
URL https://www.sciencedirect.com/science/article/pii/S0007850617301506

[6] T. Gatsos, K. A. Elsayed, Y. Zhai, D. A. Lados, Review on computational modeling of process–microstructure–property relationships in metal additive manufacturing, JOM 72 (1) (2020) 403–419. doi:10.1007/s11837-019-03913-x.
URL https://doi.org/10.1007/s11837-019-03913-x

[7] D. Dev Singh, T. Mahender, A. Raji Reddy, Powder bed fusion process: A brief review, Materials Today: Proceedings 46 (2021) 350–355, 2nd International Conference on Manufacturing Material Science and Engineering. doi:https://doi.org/10.1016/j.matpr.2020.08.415.
URL https://www.sciencedirect.com/science/article/pii/S2214785320362878

[8] P. Mair, J. Braun, L. Kaserer, L. March, D. Schimbäck, I. Letofsky-Papst, G. Leichtfried, Unique microstructure evolution of a novel ti-modified al-cu alloy processed using laser powder bed fusion, Materials Today Communications 31 (2022) 103353. doi:https://doi.org/10.1016/j.mtcomm.2022.103353.
URL https://www.sciencedirect.com/science/article/pii/S2352492822002240

[9] O. Gokcekaya, T. Ishimoto, S. Hibino, J. Yasutomi, T. Narushima, T. Nakano, Unique crystallographic texture formation in inconel 718 by laser powder bed fusion and its effect on mechanical anisotropy, Acta Materialia 212 (2021) 116876. doi:https://doi.org/10.1016/j.actamat.2021.116876.
URL https://www.sciencedirect.com/science/article/pii/S1359645421002561

[10] J. Yan, D. Zheng, H. Li, X. Jia, J. Sun, Y. Li, M. Qian, M. Yan, Selective laser melting of h13: microstructure and residual stress, Journal of Materials Science 52 (2017) 12476–12485.

[11] T. Pollock, A. Clarke, S. Babu, Design and tailoring of alloys for additive manufacturing, Metallurgical and Materials Transactions A 51 (2020) 6000–6019.

[12] N. Haghdadi, M. Laleh, M. Moyle, S. Primig, Additive manufacturing of steels: a review of achievements and challenges, Journal of Materials Science 56 (2021) 64–107.

[13] N. Kouraytem, X. Li, W. Tan, B. Kappes, A. D. Spear, Modeling process–structure–property relationships in metal additive manufacturing: a review on physics-driven versus data-driven approaches, Journal of Physics: Materials 4 (3) (2021) 032002.

[14] J. Smith, W. Xiong, W. Yan, S. Lin, P. Cheng, O. L. Kafka, G. J. Wagner, J. Cao, W. K. Liu, Linking process, structure, property, and performance for metal-based additive manufacturing: computational approaches with experimental support, Computational Mechanics 57 (4) (2016) 583–610. doi:10.1007/s00466-015-1240-4.
URL https://doi.org/10.1007/s00466-015-1240-4

[15] G. Tapia, A. Elwany, A review on process monitoring and control in metal-based additive manufacturing, Journal of Manufacturing Science and Engineering 136 (6) (2014) 060801.

[16] L. Johnson, M. Mahmoudi, B. Zhang, R. Seede, X. Huang, J. T. Maier, H. J. Maier, I. Karaman, A. Elwany, R. Arróyave, Assessing printability maps in additive manufacturing of metal alloys, Acta Materialia 176 (2019) 199–210. doi:https://doi.org/10.1016/j.actamat.2019.07.005.
URL https://www.sciencedirect.com/science/article/pii/S1359645419304355

[17] W. Wang, S. Y. Liang, Physics-based predictive model of lack-of-fusion porosity in laser powder bed fusion considering cap area, Crystals 11 (12) (2021) 1568.

[18] A. Thanki, L. Goossens, A. P. Ompusunggu, M. Bayat, A. Bey-Temsamani, B. Van Hooreweder, J.-P. Kruth, A. Witvrouw, Melt pool feature analysis using a high-speed coaxial monitoring system for laser powder bed fusion of ti-6al-4 v grade 23, The International Journal of Advanced Manufacturing Technology 120 (9-10) (2022) 6497–6514.

[19] I. Yadroitsev, A. Gusarov, I. Yadroitsava, I. Smurov, Single track formation in selective laser melting of metal powders, Journal of Materials Processing Technology 210 (12) (2010) 1624–1631.

[20] A. Dunbar, E. Denlinger, J. Heigel, P. Michaleris, P. Guerrier, R. Martukanitz, T. Simpson, Development of experimental method for in situ distortion and temperature measurements during the laser powder bed fusion additive manufacturing process, Additive Manufacturing 12 (2016) 25–30.

[21] G. Tang, B. J. Gould, A. Ngowe, A. D. Rollett, An updated index including toughness for hot-cracking susceptibility, Metallurgical and Materials Transactions A 53 (4) (2022) 1486–1498.

[22] B. Vrancken, R. K. Ganeriwala, M. J. Matthews, Analysis of laser-induced microcracking in tungsten under additive manufacturing conditions: Experiment and simulation, Acta Materialia 194 (2020) 464–472. doi:https://doi.org/10.1016/j.actamat.2020.04.060.
URL https://www.sciencedirect.com/science/article/pii/S1359645420303281

[23] M. Wirtz, J. Linke, G. Pintsuk, L. Singheiser, M. Zlobinski, Comparison of thermal shock damages induced by different simulation methods on tungsten, Journal of Nuclear Materials 438 (2013) S833–S836, proceedings of the 20th International Conference on Plasma-Surface Interactions in Controlled Fusion Devices. doi:https://doi.org/10.1016/j.jnucmat.2013.01.180.
URL https://www.sciencedirect.com/science/article/pii/S0022311513001888

[24] D. Wang, Z. Wang, K. Li, J. Ma, W. Liu, Z. Shen, Cracking in laser additively manufactured w: Initiation mechanism and a suppression approach by alloying, materials & Design 162 (2019) 384–393. doi:https://doi.org/10.1016/j.matdes.2018.12.010.
URL https://www.sciencedirect.com/science/article/pii/S0264127518308815

[25] W.-Y. Chen, X. Zhang, M. Li, R. Xu, C. Zhao, T. Sun, Laser powder bed fusion of inconel 718 on 316 stainless steel, Additive Manufacturing 36 (2020) 101500. doi:https://doi.org/10.1016/j.addma.2020.101500.
URL https://www.sciencedirect.com/science/article/pii/S2214860420308721

[26] B. Zhang, R. Seede, L. Xue, K. C. Atli, C. Zhang, A. Whitt, I. Karaman, R. Arroyave, A. Elwany, An efficient framework for printability assessment in laser powder bed fusion metal additive manufacturing, Additive Manufacturing 46 (2021) 102018. doi:https://doi.org/10.1016/j.addma.2021.102018.
URL https://www.sciencedirect.com/science/article/pii/S2214860421001834

[27] H. E. Sabzi, S. Maeng, X. Liang, M. Simonelli, N. T. Aboulkhair, P. E. Rivera-Díaz-del Castillo, Controlling crack formation and porosity in laser powder bed fusion: Alloy design and process optimisation, Additive Manufacturing 34 (2020) 101360.

[28] B. Vela, S. Mehalic, S. Sheikh, A. Elwany, I. Karaman, R. Arróyave, Evaluating the intrinsic resistance to balling of alloys: A high-throughput physics-informed and data-enabled approach, Additive Manufacturing Letters 3 (2022) 100085.

[29] S. Sheikh, B. Vela, P. Honarmandi, P. Morcos, D. Shoukr, A. M. Kotb, R. Arroyave, I. Karaman, A. Elwany, High-throughput alloy and process design for metal additive manufacturing (2023). arXiv:2304.04149.

[30] N. Shamsaei, A. Yadollahi, L. Bian, S. M. Thompson, An overview of direct laser deposition for additive manufacturing; part ii: Mechanical behavior, process parameter optimization and control, Additive manufacturing 8 (2015) 12–35.

[31] P. Morcos, D. Shoukr, T. Sundermann, T. Dobrowolski, N. Barta, J. R. Jain, R. Arróyave, I. Karaman, A. Elwany, An all-encompassing study on the joint effect of powder feedstock characteristics and manufacturing process parameters on the densification and mechanical properties of additively manufactured nickel alloy 718, Additive Manufacturing (2023) 103828doi:https://doi.org/10.1016/j.addma.2023.103828.
URL https://www.sciencedirect.com/science/article/pii/S2214860423004414

[32] R. Arróyave, D. Khatamsaz, B. Vela, R. Couperthwaite, A. Molkeri, P. Singh, D. D. Johnson, X. Qian, A. Srivastava, D. Allaire, A perspective on bayesian methods applied to materials discovery and design, MRS Communications 12 (6) (2022) 1037–1049.

[33] S. A. H. Motaman, F. Kies, P. Köhnen, M. Létang, M. Lin, A. Molotnikov, C. Haase, Optimal design for metal additive manufacturing: an integrated computational materials engineering (icme) approach, Jom 72 (2020) 1092–1104.

[34] J. H. Panchal, S. R. Kalidindi, D. L. McDowell, Key computational modeling issues in integrated computational materials engineering, Computer-Aided Design 45 (1) (2013) 4–25. doi:https://doi.org/10.1016/j.cad.2012.06.006.
URL https://www.sciencedirect.com/science/article/pii/S0010448512001352

[35] R. Pillai, Q. Q. Ren, Y.-F. Su, R. Kurfess, T. Feldhausen, S. Nag, Leveraging additive manufacturing to fabricate high temperature alloys with co-designed mechanical properties and environmental resistance, Journal of Engineering for Gas Turbines and Power (2023) 1–52doi:10.1115/1.4063784.
URL https://doi.org/10.1115/1.4063784

[36] S. Webster, H. Lin, F. M. Carter Iii, K. Ehmann, J. Cao, Physical mechanisms in hybrid additive manufacturing: A process design framework, Journal of Materials Processing Technology 291 (2021) 117048. doi:https://doi.org/10.1016/j.jmatprotec.2021.117048.
URL https://www.sciencedirect.com/science/article/pii/S092401362100008X

[37] T. W. Eagar, N. sien Tsai, Temperature fields produced by traveling distributed heat sources, 1983.
URL https://api.semanticscholar.org/CorpusID:111388870

[38] K. Karayagiz, L. Johnson, R. Seede, V. Attari, B. Zhang, X. Huang, S. Ghosh, T. Duong, I. Karaman, A. Elwany, et al., Finite interface dissipation phase field modeling of ni–nb under additive manufacturing conditions, Acta Materialia 185 (2020) 320–339.

[39] X. Huang, R. Seede, K. Karayagiz, B. Zhang, I. Karaman, A. Elwany, R. Arróyave, Hybrid microstructure-defect printability map in laser powder bed fusion additive manufacturing, Computational Materials Science 209 (2022) 111401. doi:https://doi.org/10.1016/j.commatsci.2022.111401.
URL https://www.sciencedirect.com/science/article/pii/S0927025622001719

[40] V. Attari, D. Khatamsaz, D. Allaire, R. Arroyave, Towards inverse microstructure-centered materials design using generative phase-field modeling and deep variational autoencoders, Acta Materialia 259 (2023) 119204.

[41] W. Yan, S. Lin, O. L. Kafka, Y. Lian, C. Yu, Z. Liu, J. Yan, S. Wolff, H. Wu, E. Ndip-Agbor, M. Mozaffar, K. Ehmann, J. Cao, G. J. Wagner, W. K. Liu, Data-driven multi-scale multi-physics models to derive process–structure–property relationships for additive manufacturing, Computational Mechanics 61 (5) (2018) 521–541. doi:10.1007/s00466-018-1539-z.
URL https://doi.org/10.1007/s00466-018-1539-z

[42] W. Yan, S. Lin, O. L. Kafka, C. Yu, Z. Liu, Y. Lian, S. Wolff, J. Cao, G. J. Wagner, W. K. Liu, Modeling process-structure-property relationships for additive manufacturing, Frontiers of Mechanical Engineering 13 (2018) 482–492.

[43] A. E. Wilson-Heid, S. Qin, A. M. Beese, Multiaxial plasticity and fracture behavior of stainless steel 316l by laser powder bed fusion: Experiments and computational modeling, Acta Materialia 199 (2020) 578–592.

[44] R. Seede, D. Shoukr, B. Zhang, A. Whitt, S. Gibbons, P. Flater, A. Elwany, R. Arroyave, I. Karaman, An ultra-high strength martensitic steel fabricated using selective laser melting additive manufacturing: Densification, microstructure, and mechanical properties, Acta Materialia 186 (2020) 199–214. doi:https://doi.org/10.1016/j.actamat.2019.12.037.
URL https://www.sciencedirect.com/science/article/pii/S1359645419308766

[45] M. Tang, P. C. Pistorius, J. L. Beuth, Prediction of lack-of-fusion porosity for powder bed fusion, Additive Manufacturing 14 (2017) 39–48.

[46] S. A. Khairallah, A. T. Anderson, A. Rubenchik, W. E. King, Laser powder-bed fusion additive manufacturing: Physics of complex melt flow and formation mechanisms of pores, spatter, and denudation zones, Acta Materialia 108 (2016) 36–45.

[47] D. Zhang, S. Sun, D. Qiu, M. A. Gibson, M. S. Dargusch, M. Brandt, M. Qian, M. Easton, Metal alloys for fusion-based additive manufacturing, Advanced Engineering Materials 20 (5) (2018) 1700952. arXiv:https://onlinelibrary.wiley.com/doi/pdf/10.1002/adem.201700952, doi:https://doi.org/10.1002/adem.201700952.
URL https://onlinelibrary.wiley.com/doi/abs/10.1002/adem.201700952

[48] B. A. Fulcher, D. K. Leigh, T. J. Watt, Comparison of alsi10mg and al 6061 processed through dmls, in: 2014 International Solid Freeform Fabrication Symposium, University of Texas at Austin, 2014.

[49] A. Suzuki, H. Inui, T. M. Pollock, L12-strengthened cobalt-base superalloys, Annual Review of Materials Research 45 (1) (2015) 345–368. arXiv:https://doi.org/10.1146/annurev-matsci-070214-021043, doi:10.1146/annurev-matsci-070214-021043.
URL https://doi.org/10.1146/annurev-matsci-070214-021043

[50] M. Tsunekane, A. Suzuki, T. M. Pollock, Single-crystal solidification of new co–al–w-base alloys, Intermetallics 19 (5) (2011) 636–643.

[51] T. Clyne, D. GJ, The influence of composition on solidification cracking susceptibility in binary alloy systems (1981).

[52] M. Rappaz, J. M. Drezet, M. Gremaud, A new hot-tearing criterion, Metallurgical and materials transactions A 30 (1999) 449–455.

[53] M. B. Djurdjevic, G. Huber, Determination of rigidity point/temperature using thermal analysis method and mechanical technique, Journal of Alloys and Compounds 590 (2014) 500–506. doi:https://doi.org/10.1016/j.jallcom.2013.11.020.
URL https://www.sciencedirect.com/science/article/pii/S0925838813027503

[54] S. Kou, A criterion for cracking during solidification, Acta Materialia 88 (2015) 366–374.

[55] M. A. Easton, M. A. Gibson, S. Zhu, T. B. Abbott, An a priori hot-tearing indicator applied to die-cast magnesium-rare earth alloys, Metallurgical and Materials Transactions A 45 (2014) 3586–3595.

[56] Suyitno, W. Kool, L. Katgerman, Hot tearing criteria evaluation for direct-chill casting of an al-4.5 pct cu alloy, Metallurgical and Materials Transactions A 36 (2005) 1537–1546.

[57] Z. Gan, O. L. Kafka, N. Parab, C. Zhao, L. Fang, O. Heinonen, T. Sun, W. K. Liu, Universal scaling laws of keyhole stability and porosity in 3d printing of metals, Nature communications 12 (1) (2021) 2379.

[58] M. Thomas, G. J. Baxter, I. Todd, Normalised model-based processing diagrams for additive layer manufacture of engineering alloys, Acta Materialia 108 (2016) 26–35. doi:https://doi.org/10.1016/j.actamat.2016.02.025.
URL https://www.sciencedirect.com/science/article/pii/S1359645416300994

[59] B. Rankouhi, A. K. Agrawal, F. E. Pfefferkorn, D. J. Thoma, A dimensionless number for predicting universal processing parameter boundaries in metal powder bed additive manufacturing, Manufacturing Letters 27 (2021) 13–17. doi:https://doi.org/10.1016/j.mfglet.2020.12.002.
URL https://www.sciencedirect.com/science/article/pii/S2213846320301735

[60] H. E. Sabzi, S. Maeng, X. Liang, M. Simonelli, N. T. Aboulkhair, P. E. R.-D. del Castillo, Controlling crack formation and porosity in laser powder bed fusion: Alloy design and process optimisation, Additive Manufacturing 34 (2020) 101360. doi:https://doi.org/10.1016/j.addma.2020.101360.
URL https://www.sciencedirect.com/science/article/pii/S2214860420307326

[61] A. M. Rubenchik, W. E. King, S. S. Wu, Scaling laws for the additive manufacturing, Journal of Materials Processing Technology 257 (2018) 234–243. doi:https://doi.org/10.1016/j.jmatprotec.2018.02.034.
URL https://www.sciencedirect.com/science/article/pii/S0924013618300906

[62] X. Zhou, X. Liu, D. Zhang, Z. Shen, W. Liu, Balling phenomena in selective laser melted tungsten, Journal of Materials Processing Technology 222 (2015) 33–42. doi:https://doi.org/10.1016/j.jmatprotec.2015.02.032.
URL https://www.sciencedirect.com/science/article/pii/S0924013615000825

[63] D. Schuöcker, Handbook of the EuroLaser academy, Vol. 2, Springer Science & Business Media, 1998.

[64] J. H. Martin, B. D. Yahata, J. M. Hundley, J. A. Mayer, T. A. Schaedler, T. M. Pollock, 3d printing of high-strength aluminium alloys, Nature 549 (7672) (2017) 365–369.

[65] J. Liu, P. Hu, S. Kou, A cfd study on intergranular liquid feeding and cracking during solidification in welding, Metallurgical and Materials Transactions A (2023) 1–14.

[66] M. J. Bermingham, D. H. StJohn, J. Krynen, S. Tedman-Jones, M. S. Dargusch, Promoting the columnar to equiaxed transition and grain refinement of titanium alloys during additive manufacturing, Acta Materialia 168 (2019) 261–274. doi:https://doi.org/10.1016/j.actamat.2019.02.020.
URL https://www.sciencedirect.com/science/article/pii/S1359645419301065

[67] Z. Sun, X. P. Tan, M. Descoins, D. Mangelinck, S. B. Tor, C. S. Lim, Revealing hot tearing mechanism for an additively manufactured high-entropy alloy via selective laser melting, Scripta Materialia 168 (2019) 129–133.

[68] Z. Sun, X. Tan, C. Wang, M. Descoins, D. Mangelinck, S. B. Tor, E. A. Jägle, S. Zaefferer, D. Raabe, Reducing hot tearing by grain boundary segregation engineering in additive manufacturing: example of an alxcocrfeni high-entropy alloy, Acta Materialia 204 (2021) 116505. doi:https://doi.org/10.1016/j.actamat.2020.116505.
URL https://www.sciencedirect.com/science/article/pii/S1359645420309307

[69] C. Guo, S. Wei, Z. Wu, P. Wang, B. Zhang, U. Ramamurty, X. Qu, Effect of dual phase structure induced by chemical segregation on hot tearing reduction in additive manufacturing, materials & Design 228 (2023) 111847. doi:https://doi.org/10.1016/j.matdes.2023.111847.
URL https://www.sciencedirect.com/science/article/pii/S0264127523002629

[70] J. Schrier, A. J. Norquist, T. Buonassisi, J. Brgoch, In pursuit of the exceptional: Research directions for machine learning in chemical and materials science, Journal of the American Chemical Society 145 (40) (2023) 21699–21716, doi: 10.1021/jacs.3c04783. doi:10.1021/jacs.3c04783.
URL https://doi.org/10.1021/jacs.3c04783

[71] T. Wilkinson, M. Casata, D. Barba, Automatic process mapping for ti64 single tracks in laser powder bed fusion, in: S. Wagstaff, A. Anderson, A. S. Sabau (Eds.), Materials Processing Fundamentals 2023, Springer Nature Switzerland, Cham, 2023, pp. 199–209.

[72] W. Zhang, B. Abranovic, J. Hanson-Regalado, C. Koz, B. Duvvuri, K. Shimada, J. Beuth, L. B. Kara, Flaw detection in metal additive manufacturing using deep learned acoustic features, in: Workshop of conference on neural information processing systems, 2020.

[73] C. Zhang, L. Xue, K. C. Atli, R. Arróyave, I. Karaman, A. Elwany, On the Fabrication of Defect-Free Nickel-Rich Nickel–Titanium Parts Using Laser Powder Bed Fusion, Journal of Manufacturing Science and Engineering 144 (9) (2022) 091011. arXiv:https://asmedigitalcollection.asme.org/manufacturingscience/article-pdf/144/9/091011/6901568/manu_144_9_091011.pdf, doi:10.1115/1.4054935.
URL https://doi.org/10.1115/1.4054935

[74] V. Juechter, T. Scharowsky, R. Singer, C. Körner, Processing window and evaporation phenomena for ti–6al–4v produced by selective electron beam melting, Acta Materialia 76 (2014) 252–258. doi:https://doi.org/10.1016/j.actamat.2014.05.037.
URL https://www.sciencedirect.com/science/article/pii/S1359645414003851

[75] T. Childs, C. Hauser, M. Badrossamay, Mapping and modelling single scan track formation in direct metal selective laser melting, CIRP Annals 53 (1) (2004) 191–194. doi:https://doi.org/10.1016/S0007-8506(07)60676-3.
URL https://www.sciencedirect.com/science/article/pii/S0007850607606763

[76] C. Zhang, L. Xue, S. A. Pestka, M. Ranaiefar, K. C. Atli, P. Honarmandi, R. Arróyave, I. Karaman, A. Elwany, Processing parameters and martensitic phase transformation relationships in near defect-free additively manufactured nitihf high temperature shape memory alloys, Materials & Design 222 (2022) 110988. doi:https://doi.org/10.1016/j.matdes.2022.110988.
URL https://www.sciencedirect.com/science/article/pii/S0264127522006104

[77] R. Seede, A. Whitt, J. Ye, S. Gibbons, P. Flater, B. Gaskey, A. Elwany, R. Arroyave, I. Karaman, A lightweight fe–mn–al–c austenitic steel with ultra-high strength and ductility fabricated via laser powder bed fusion, Materials Science and Engineering: A 874 (2023) 145007. doi:https://doi.org/10.1016/j.msea.2023.145007.
URL https://www.sciencedirect.com/science/article/pii/S0921509323004318

[78] D. Shoukr, P. Morcos, T. Sundermann, T. Dobrowolski, C. Yates, J. R. Jain, R. Arróyave, I. Karaman, A. Elwany, Influence of layer thickness on the printability of nickel alloy 718:a systematic process optimization framework, Additive Manufacturing 73 (2023) 103646. doi:https://doi.org/10.1016/j.addma.2023.103646.
URL https://www.sciencedirect.com/science/article/pii/S2214860423002592

[79] A. K. Agrawal, B. Rankouhi, D. J. Thoma, Predictive process mapping for laser powder bed fusion: A review of existing analytical solutions, Current Opinion in Solid State and Materials Science 26 (6) (2022) 101024. doi:https://doi.org/10.1016/j.cossms.2022.101024.
URL https://www.sciencedirect.com/science/article/pii/S1359028622000444

[80] S. Sheikh, M. Ranaiefar, P. Honarmandi, B. Vela, P. Morcos, D. Shoukr, R. Arroyave, I. Karaman, A. Elwany, An automated fully-computational framework to construct printability maps for additively manufactured metal alloys, arXiv preprint arXiv:2304.04113 (2023).

[81] G. G. Gladush, I. Smurov, Physics of laser materials processing: theory and experiment, Vol. 146, Springer Science & Business Media, 2011.

[82] J.-N. Zhu, E. Borisov, X. Liang, E. Farber, M. Hermans, V. Popovich, Predictive analytical modelling and experimental validation of processing maps in additive manufacturing of nitinol alloys, Additive Manufacturing 38 (2021) 101802.

[83] W. E. King, H. D. Barth, V. M. Castillo, G. F. Gallegos, J. W. Gibbs, D. E. Hahn, C. Kamath, A. M. Rubenchik, Observation of keyhole-mode laser melting in laser powder-bed fusion additive manufacturing, Journal of Materials Processing Technology 214 (12) (2014) 2915–2925. doi:https://doi.org/10.1016/j.jmatprotec.2014.06.005.
URL https://www.sciencedirect.com/science/article/pii/S0924013614002283

[84] J. J. Lewandowski, M. Seifi, Metal additive manufacturing: a review of mechanical properties, Annual review of materials research 46 (2016) 151–186.

[85] G. Tapia, W. King, L. Johnson, R. Arroyave, I. Karaman, A. Elwany, Uncertainty propagation analysis of computational models in laser powder bed fusion additive manufacturing using polynomial chaos expansions, Journal of Manufacturing Science and Engineering 140 (12) (2018) 121006.

[86] Z. Wang, X. Lin, N. Kang, J. Chen, Y. Tang, H. Tan, X. Yu, H. Yang, W. Huang, Directed energy deposition additive manufacturing of a sc/zr-modified al–mg alloy: Effect of thermal history on microstructural evolution and mechanical properties, Materials Science and Engineering: A 802 (2021) 140606.

[87] Z. Wang, W. Yan, W. K. Liu, M. Liu, Powder-scale multi-physics modeling of multi-layer multi-track selective laser melting with sharp interface capturing method, Computational Mechanics 63 (2019) 649–661.

[88] A. F. Chadwick, P. W. Voorhees, The development of grain structure during additive manufacturing, Acta Materialia 211 (2021) 116862.

[89] X. Huang, R. Seede, K. Karayagiz, A. Whitt, B. Zhang, J. Ye, I. Karaman, A. Elwany, R. Arroyave, Predictive microstructure distribution and printability maps in laser powder bed fusion for a ni-cu alloy, Accepted for publication in Computational Materials Science.

[90] W. . Kurz, B. Giovanola, R. Trivedi, Theory of microstructural development during rapid solidification, Acta metallurgica 34 (5) (1986) 823–830.

[91] J. Berry, A. Perron, J.-L. Fattebert, J. D. Roehling, B. Vrancken, T. T. Roehling, D. L. Rosas, J. A. Turner, S. A. Khairallah, J. T. McKeown, et al., Toward multiscale simulations of tailored microstructure formation in metal additive manufacturing, Materials Today 51 (2021) 65–86.

[92] J. Soderlind, A. A. Martin, N. P. Calta, P. J. DePond, J. Wang, B. Vrancken, R. E. Schäublin, I. Basu, V. Thampy, A. Y. Fong, et al., Melt-pool dynamics and microstructure of mg alloy we43 under laser powder bed fusion additive manufacturing conditions, Crystals 12 (10) (2022) 1437.

[93] M. F. Ashby, D. CEBON, Materials selection in mechanical design, Le Journal de Physique IV 3 (C7) (1993) C7–1.

[94] D. Mies, W. Marsden, S. Warde, Overview of additive manufacturing informatics: "a digital thread", Integrating Materials and Manufacturing Innovation 5 (1) (2016) 114–142. doi:10.1186/s40192-016-0050-7.
URL https://doi.org/10.1186/s40192-016-0050-7

[95] S. L. Sing, C. Kuo, C. Shih, C. Ho, C. K. Chua, Perspectives of using machine learning in laser powder bed fusion for metal additive manufacturing, Virtual and Physical Prototyping 16 (3) (2021) 372–386.

[96] A. Jain, S. P. Ong, G. Hautier, W. Chen, W. D. Richards, S. Dacek, S. Cholia, D. Gunter, D. Skinner, G. Ceder, et al., Commentary: The materials project: A materials genome approach to accelerating materials innovation, APL materials 1 (1) (2013).

[97] S. Curtarolo, W. Setyawan, G. L. Hart, M. Jahnatek, R. V. Chepulskii, R. H. Taylor, S. Wang, J. Xue, K. Yang, O. Levy, M. J. Mehl, H. T. Stokes, D. O. Demchenko, D. Morgan, Aflow: An automatic framework for high-throughput materials discovery, Computational Materials Science 58 (2012) 218–226. doi:https://doi.org/10.1016/j.commatsci.2012.02.005.
URL https://www.sciencedirect.com/science/article/pii/S0927025612000717

[98] P. Lambrix, R. Armiento, A. Delin, H. Li, Fair big data in the materials design domain, Encyclopedia of Big Data Technologies, AY Zomaya, J. Taheri and S. Sakr, eds, Springer, Cham (2022).

[99] M. Axton, A. Baak, N. Blomberg, J.-W. Boiten, L. B. da Silva Santos, P. E. Bourne, J. Bouwman, A. J. Brookes, T. Clark, et al., The fair guiding principles for scientific data management and stewardship, Scientific data 3 (2016) 160018.

[100] W. Yuan, Z. Liang, Effect of zr addition on properties of al–mg–si aluminum alloy used for all aluminum alloy conductor, Materials & Design 32 (8-9) (2011) 4195–4200.

[101] H. Irrinki, M. Dexter, B. Barmore, R. Enneti, S. Pasebani, S. Badwe, J. Stitzel, R. Malhotra, S. V. Atre, Effects of powder attributes and laser powder bed fusion (l-pbf) process conditions on the densification and mechanical properties of 17-4 ph stainless steel, Jom 68 (2016) 860–868.

[102] S. Vock, B. Klöden, A. Kirchner, T. Weißgärber, B. Kieback, Powders for powder bed fusion: a review, Progress in Additive Manufacturing 4 (2019) 383–397.

[103] A. Soltani-Tehrani, M. Habibnejad-Korayem, S. Shao, M. Haghshenas, N. Shamsaei, Ti-6al-4v powder characteristics in laser powder bed fusion: The effect on tensile and fatigue behavior, Additive Manufacturing 51 (2022) 102584.

[104] X. Lu, W. Zhang, M. Chiumenti, M. Cervera, B. Gillham, P. Yu, S. Yin, X. Lin, R. P. Babu, R. Lupoi, Crack-free laser powder bed fusion by substrate design, Additive Manufacturing 59 (2022) 103149.

[105] S. Z. Uddin, L. E. Murr, C. A. Terrazas, P. Morton, D. A. Roberson, R. B. Wicker, Processing and characterization of crack-free aluminum 6061 using high-temperature heating in laser powder bed fusion additive manufacturing, Additive Manufacturing 22 (2018) 405–415.

[106] W. Stopyra, K. Gruber, I. Smolina, T. Kurzynowski, B. Kuźnicka, Laser powder bed fusion of aa7075 alloy: Influence of process parameters on porosity and hot cracking, Additive Manufacturing 35 (2020) 101270.

[107] P. Hanzl, M. Zetek, T. Bakša, T. Kroupa, The influence of processing parameters on the mechanical properties of slm parts, Procedia Engineering 100 (2015) 1405–1413.

[108] A. Khorasani, I. Gibson, U. S. Awan, A. Ghaderi, The effect of slm process parameters on density, hardness, tensile strength and surface quality of ti-6al-4v, Additive manufacturing 25 (2019) 176–186.

[109] Y. Lu, P. Witherell, A. Donmez, A collaborative data management system for additive manufacturing, in: International design engineering technical conferences and computers and information in engineering conference, Vol. 58110, American Society of Mechanical Engineers, 2017, p. V001T02A036.

[110] T. Prater, Database development for additive manufacturing, Progress in Additive Manufacturing 2 (1) (2017) 11–18. doi:10.1007/s40964-017-0016-0.
URL https://doi.org/10.1007/s40964-017-0016-0

[111] S. B. Maidin, I. Campbell, E. Pei, Development of a design feature database to support design for additive manufacturing, Assembly Automation (2012).

[112] A. Y.-T. Wang, R. J. Murdock, S. K. Kauwe, A. O. Oliynyk, A. Gurlo, J. Brgoch, K. A. Persson, T. D. Sparks, Machine learning for materials scientists: an introductory guide toward best practices, Chemistry of Materials 32 (12) (2020) 4954–4965.

[113] G. E. Batista, M. C. Monard, An analysis of four missing data treatment methods for supervised learning, Applied artificial intelligence 17 (5-6) (2003) 519–533.

[114] G. Chhabra, V. Vashisht, J. Ranjan, A comparison of multiple imputation methods for data with missing values, Indian Journal of Science and Technology 10 (19) (2017) 1–7.

[115] M. J. Azur, E. A. Stuart, C. Frangakis, P. J. Leaf, Multiple imputation by chained equations: what is it and how does it work?, International journal of methods in psychiatric research 20 (1) (2011) 40–49.

[116] F. Tang, H. Ishwaran, Random forest missing data algorithms, Statistical Analysis and Data Mining: The ASA Data Science Journal 10 (6) (2017) 363–377.

[117] H. Zahed, Bayesian treatment of missing data using multiple imputation, EPPS 7390 (2013) 1–243.

[118] S. Karumuri, Z. D. McClure, A. Strachan, M. Titus, I. Bilionis, Hierarchical bayesian approach to experimental data fusion: Application to strength prediction of high entropy alloys from hardness measurements, Computational Materials Science 217 (2023) 111851.

[119] B. Vela, D. Khatamsaz, C. Acemi, I. Karaman, R. Arróyave, Data-augmented modeling for yield strength of refractory high entropy alloys: A bayesian approach, Acta Materialia (2023) 119351.

[120] M. Safdar, G. Lamouche, P. P. Paul, G. Wood, Y. F. Zhao, Feature engineering in additive manufacturing, in: Engineering of Additive Manufacturing Features for Data-Driven Solutions: Sources, Techniques, Pipelines, and Applications, Springer, 2023, pp. 17–43.

[121] M. Valizadeh, S. J. Wolff, Convolutional neural network applications in additive manufacturing: A review, Advances in Industrial and Manufacturing Engineering 4 (2022) 100072.

[122] I. Cohen, Y. Huang, J. Chen, J. Benesty, J. Benesty, J. Chen, Y. Huang, I. Cohen, Pearson correlation coefficient, Noise reduction in speech processing (2009) 1–4.

[123] J. H. Zar, Spearman rank correlation, Encyclopedia of biostatistics 7 (2005).

[124] M. Sanderson, I. Soboroff, Problems with kendall's tau, in: Proceedings of the 30th annual international ACM SIGIR conference on Research and development in information retrieval, 2007, pp. 839–840.

[125] N. Hoque, D. K. Bhattacharyya, J. K. Kalita, Mifs-nd: A mutual information-based feature selection method, Expert Systems with Applications 41 (14) (2014) 6371–6385.

[126] S. Liu, B. B. Kappes, B. Amin-ahmadi, O. Benafan, X. Zhang, A. P. Stebner, Physics-informed machine learning for composition–process–property design: Shape memory alloy demonstration, Applied Materials Today 22 (2021) 100898.

[127] Y. Zhang, C. Ling, A strategy to apply machine learning to small datasets in materials science, Npj Computational Materials 4 (1) (2018) 25.

[128] J. Liu, J. Ye, D. Silva Izquierdo, A. Vinel, N. Shamsaei, S. Shao, A review of machine learning techniques for process and performance optimization in laser beam powder bed fusion additive manufacturing, Journal of Intelligent Manufacturing (2022) 1–27.

[129] L. Van der Maaten, G. Hinton, Visualizing data using t-sne., Journal of machine learning research 9 (11) (2008).

[130] T. Kirk, B. Vela, S. Mehalic, K. Youssef, R. Arróyave, Entropy-driven melting point depression in fcc heas, Scripta Materialia 208 (2022) 114336.

[131] Y. Tan, J. Zhang, X. Li, Y. Xu, C.-Y. Wu, Comprehensive evaluation of powder flowability for additive manufacturing using principal component analysis, Powder Technology 393 (2021) 154–164.

[132] A. Brenning, Transforming feature space to interpret machine learning models, arXiv preprint arXiv:2104.04295 (2021).

[133] Y. Zhang, G. S. Hong, D. Ye, K. Zhu, J. Y. Fuh, Extraction and evaluation of melt pool, plume and spatter information for powder-bed fusion am process monitoring, Materials & Design 156 (2018) 458–469.

[134] A. Suzuki, Y. Shiba, H. Ibe, N. Takata, M. Kobashi, Machine-learning assisted optimization of process parameters for controlling the microstructure in a laser powder bed fused wc/co cemented carbide, Additive Manufacturing 59 (2022) 103089.

[135] L. McInnes, J. Healy, J. Melville, Umap: Uniform manifold approximation and projection for dimension reduction, arXiv preprint arXiv:1802.03426 (2018).

[136] T. Z. Khan, T. Kirk, G. Vazquez, P. Singh, A. Smirnov, D. D. Johnson, K. Youssef, R. Arróyave, Towards stacking fault energy engineering in fcc high entropy alloys, Acta Materialia 224 (2022) 117472.

[137] D. Khatamsaz, B. Vela, P. Singh, D. D. Johnson, D. Allaire, R. Arróyave, Multi-objective materials bayesian optimization with active learning of design constraints: Design of ductile refractory multi-principal-element alloys, Acta Materialia 236 (2022) 118133.

[138] B. Vela, C. Acemi, P. Singh, T. Kirk, W. Trehern, E. Norris, D. D. Johnson, I. Karaman, R. Arróyave, High-throughput exploration of the wmovtanbal refractory multi-principal-element alloys under multiple-property constraints, Acta Materialia 248 (2023) 118784.

[139] I. T. Jolliffe, Discarding variables in a principal component analysis. i: Artificial data, Journal of the Royal Statistical Society Series C: Applied Statistics 21 (2) (1972) 160–173.

[140] I. T. Jolliffe, Discarding variables in a principal component analysis. ii: Real data, Journal of the Royal Statistical Society Series C: Applied Statistics 22 (1) (1973) 21–31.

[141] I. T. Jolliffe, Principal component analysis for special types of data, Springer, 2002.

[142] Q. Guo, W. Wu, D. Massart, C. Boucon, S. de Jong, Feature selection in principal component analysis of analytical data, Chemometrics and Intelligent Laboratory Systems 61 (1-2) (2002) 123–132.

[143] R. Wong, A. Tran, B. Dovgyy, C. S. Maldonado, M.-S. Pham, Meta-analysis of literature data in metal additive manufacturing: What can we (and the machine) learn from reported data?, arXiv preprint arXiv:2308.16621 (2023).

[144] J. Cadima, I. T. Jolliffe, Loading and correlations in the interpretation of principle compenents, Journal of applied Statistics 22 (2) (1995) 203–214.

[145] S. M. Lundberg, S.-I. Lee, A unified approach to interpreting model predictions, Advances in neural information processing systems 30 (2017).

[146] M. T. Ribeiro, S. Singh, C. Guestrin, " why should i trust you?" explaining the predictions of any classifier, in: Proceedings of the 22nd ACM SIGKDD international conference on knowledge discovery and data mining, 2016, pp. 1135–1144.

[147] Q. Liu, H. Wu, M. J. Paul, P. He, Z. Peng, B. Gludovatz, J. J. Kruzic, C. H. Wang, X. Li, Machine-learning assisted laser powder bed fusion process optimization for alsi10mg: New microstructure description indices and fracture mechanisms, Acta Materialia 201 (2020) 316–328.

[148] P. Akbari, F. Ogoke, N.-Y. Kao, K. Meidani, C.-Y. Yeh, W. Lee, A. B. Farimani, Meltpoolnet: Melt pool characteristic prediction in metal additive manufacturing using machine learning, Additive Manufacturing 55 (2022) 102817.

[149] Z. Xiang, M. Fan, G. V. Tovar, W. Trehern, B.-J. Yoon, X. Qian, R. Arroyave, X. Qian, Physics-constrained automatic feature engineering for predictive modeling in materials science, in: Proceedings of the AAAI Conference on Artificial Intelligence, Vol. 35, 2021, pp. 10414–10421.

[150] S. Mojumder, Z. Gan, Y. Li, A. Al Amin, W. K. Liu, Linking process parameters with lack-of-fusion porosity for laser powder bed fusion metal additive manufacturing, Additive Manufacturing 68 (2023) 103500.

[151] M. Schmidt, H. Lipson, Distilling free-form natural laws from experimental data, science 324 (5923) (2009) 81–85.

[152] R. Dubčáková, Eureqa: software review (2011).

[153] S.-M. Udrescu, M. Tegmark, Ai feynman: A physics-inspired method for symbolic regression, Science Advances 6 (16) (2020) eaay2631.

[154] A.-C. Lee, R.-Y. Huang, T.-D. Nguyen, C.-W. Cheng, M.-C. Tsai, Laser powder bed fusion of multilayer thin-walled structures based on data-driven model, Journal of Laser Micro Nanoengineering 15 (1) (2020) 1–7.

[155] B. Shen, W. Xie, Z. J. Kong, Clustered discriminant regression for high-dimensional data feature extraction and its applications in healthcare and additive manufacturing, IEEE Transactions on Automation Science and Engineering 18 (4) (2020) 1998–2010.

[156] R. Ouyang, S. Curtarolo, E. Ahmetcik, M. Scheffler, L. M. Ghiringhelli, Sisso: A compressed-sensing method for identifying the best low-dimensional descriptor in an immensity of offered candidates, Physical Review Materials 2 (8) (2018) 083802.

[157] P. Singh, T. Del Rose, G. Vazquez, R. Arroyave, Y. Mudryk, Machine-learning enabled thermodynamic model for the design of new rare-earth compounds, Acta Materialia 229 (2022) 117759.

[158] A. J. Summers, H. Yin, R. D. Fischer, B. C. Prorok, X. Lou, Q. P. He, Constructing process maps for pulsed wave laser additive manufacturing with interpretable machine learning, Journal of Manufacturing Processes 104 (2023) 138–149.

[159] X. Yao, S. K. Moon, G. Bi, A hybrid machine learning approach for additive manufacturing design feature recommendation, Rapid Prototyping Journal 23 (6) (2017) 983–997.

[160] Y. LeCun, Y. Bengio, G. Hinton, Deep learning, nature 521 (7553) (2015) 436–444.

[161] L. Ward, A. Agrawal, A. Choudhary, C. Wolverton, A general-purpose machine learning framework for predicting properties of inorganic materials, npj Computational Materials 2 (1) (2016) 1–7.

[162] A. Agrawal, A. Choudhary, Deep materials informatics: Applications of deep learning in materials science, Mrs Communications 9 (3) (2019) 779–792.

[163] K. T. Butler, D. W. Davies, H. Cartwright, O. Isayev, A. Walsh, Machine learning for molecular and materials science, Nature 559 (7715) (2018) 547–555.

[164] D. T. Fullwood, S. R. Niezgoda, B. L. Adams, S. R. Kalidindi, Microstructure sensitive design for performance optimization, Progress in Materials Science 55 (6) (2010) 477–562.

[165] S. Shao, M. M. Khonsari, S. Guo, W. J. Meng, N. Li, Overview: additive manufacturing enabled accelerated design of ni-based alloys for improved fatigue life, Additive Manufacturing 29 (2019) 100779.

[166] Y. T. Tang, C. Panwisawas, J. N. Ghoussoub, Y. Gong, J. W. Clark, A. A. Németh, D. G. McCartney, R. C. Reed, Alloys-by-design: Application to new superalloys for additive manufacturing, Acta Materialia 202 (2021) 417–436.

[167] N. Despres, E. Cyr, P. Setoodeh, M. Mohammadi, Deep learning and design for additive manufacturing: a framework for microlattice architecture, Jom 72 (2020) 2408–2418.

[168] Y. Kim, Y. Kim, C. Yang, K. Park, G. X. Gu, S. Ryu, Deep learning framework for material design space exploration using active transfer learning and data augmentation, npj Computational Materials 7 (1) (2021) 140.

[169] R. M. Yazdi, F. Imani, H. Yang, A hybrid deep learning model of process-build interactions in additive manufacturing, Journal of Manufacturing Systems 57 (2020) 460–468.

[170] Z. Snow, B. Diehl, E. W. Reutzel, A. Nassar, Toward in-situ flaw detection in laser powder bed fusion additive manufacturing through layerwise imagery and machine learning, Journal of Manufacturing Systems 59 (2021) 12–26.

[171] H. Baumgartl, J. Tomas, R. Buettner, M. Merkel, A deep learning-based model for defect detection in laser-powder bed fusion using in-situ thermographic monitoring, Progress in Additive Manufacturing 5 (3) (2020) 277–285.

[172] S. A. Shevchik, G. Masinelli, C. Kenel, C. Leinenbach, K. Wasmer, Deep learning for in situ and real-time quality monitoring in additive manufacturing using acoustic emission, IEEE Transactions on Industrial Informatics 15 (9) (2019) 5194–5203.

[173] Z. Yang, Y. Lu, H. Yeung, S. Krishnamurty, Investigation of deep learning for real-time melt pool classification in additive manufacturing, in: 2019 IEEE 15th international conference on automation science and engineering (CASE), IEEE, 2019, pp. 640–647.

[174] X. Li, X. Jia, Q. Yang, J. Lee, Quality analysis in metal additive manufacturing with deep learning, Journal of Intelligent Manufacturing 31 (2020) 2003–2017.

[175] B. Ahuja, M. Karg, M. Schmidt, Additive manufacturing in production: challenges and opportunities, Laser 3d manufacturing II 9353 (2015) 11–20.

[176] Y. Du, T. Mukherjee, T. DebRoy, Physics-informed machine learning and mechanistic modeling of additive manufacturing to reduce defects, Applied Materials Today 24 (2021) 101123.

[177] J. Ye, M. Mahmoudi, K. Karayagiz, L. Johnson, R. Seede, I. Karaman, R. Arroyave, A. Elwany, Bayesian calibration of multiple coupled simulation models for metal additive manufacturing: A bayesian network approach, ASCE-ASME Journal of Risk and Uncertainty in Engineering Systems, Part B: Mechanical Engineering 8 (1) (2022) 011111.

[178] M. Mahmoudi, G. Tapia, K. Karayagiz, B. Franco, J. Ma, R. Arroyave, I. Karaman, A. Elwany, Multivariate calibration and experimental validation of a 3d finite element thermal model for laser powder bed fusion metal additive manufacturing, Integrating Materials and Manufacturing Innovation 7 (2018) 116–135.

[179] U. F. Ghumman, L. Fang, G. J. Wagner, W. Chen, Calibration of Cellular Automaton Model for Microstructure Prediction in Additive Manufacturing Using Dissimilarity Score, Journal of Manufacturing Science and Engineering 145 (6) (2023) 061002. arXiv:https://asmedigitalcollection.asme.org/manufacturingscience/article-pdf/145/6/061002/6989369/manu_145_6_061002.pdf, doi:10.1115/1.4056690.
URL https://doi.org/10.1115/1.4056690

[180] Y. Lian, S. Lin, W. Yan, W. K. Liu, G. J. Wagner, A parallelized three-dimensional cellular automaton model for grain growth during additive manufacturing, Computational Mechanics 61 (2018) 543–558.

[181] M. I. Latypov, M. Kühbach, I. J. Beyerlein, J.-C. Stinville, L. S. Toth, T. M. Pollock, S. R. Kalidindi, Application of chord length distributions and principal component analysis for quantification and representation of diverse polycrystalline microstructures, Materials Characterization 145 (2018) 671–685. doi:https://doi.org/10.1016/j.matchar.2018.09.020.
URL https://www.sciencedirect.com/science/article/pii/S1044580318313743

[182] J. R. Deneault, J. Chang, J. Myung, D. Hooper, A. Armstrong, M. Pitt, B. Maruyama, Toward autonomous additive manufacturing: Bayesian optimization on a 3d printer, MRS Bulletin 46 (2021) 566–575.

[183] J. H. Montoya, K. T. Winther, R. A. Flores, T. Bligaard, J. S. Hummelshøj, M. Aykol, Autonomous intelligent agents for accelerated materials discovery, Chem. Sci. 11 (2020) 8517–8532. doi:10.1039/D0SC01101K.
URL http://dx.doi.org/10.1039/D0SC01101K

[184] M. M. Noack, G. S. Doerk, R. Li, J. K. Streit, R. A. Vaia, K. G. Yager, M. Fukuto, Autonomous materials discovery driven by gaussian process regression with inhomogeneous measurement noise and anisotropic kernels, Scientific reports 10 (1) (2020) 17663.

[185] S. T. Bukkapatnam, Autonomous materials discovery and manufacturing (amdm): A review and perspectives, IISE Transactions 55 (1) (2023) 75–93.

[186] B. P. MacLeod, F. G. L. Parlane, C. C. Rupnow, K. E. Dettelbach, M. S. Elliott, T. D. Morrissey, T. H. Haley, O. Proskurin, M. B. Rooney, N. Taherimakhsousi, D. J. Dvorak, H. N. Chiu, C. E. B. Waizenegger, K. Ocean, M. Mokhtari, C. P. Berlinguette, A self-driving laboratory advances the pareto front for material properties, Nature Communications 13 (1) (2022) 995. doi:10.1038/s41467-022-28580-6.
URL https://doi.org/10.1038/s41467-022-28580-6

[187] B. P. MacLeod, F. G. Parlane, T. D. Morrissey, F. Häse, L. M. Roch, K. E. Dettelbach, R. Moreira, L. P. Yunker, M. B. Rooney, J. R. Deeth, Self-driving laboratory for accelerated discovery of thin-film materials, Science Advances 6 (20) (2020) eaaz8867.

[188] H. Gao, S. Zhong, W. Zhang, T. Igou, E. Berger, E. Reid, Y. Zhao, D. Lambeth, L. Gan, M. A. Afolabi, et al., Revolutionizing membrane design using machine learning-bayesian optimization, Environmental Science & Technology 56 (4) (2021) 2572–2581.

[189] K. Wang, A. W. Dowling, Bayesian optimization for chemical products and functional materials, Current Opinion in Chemical Engineering 36 (2022) 100728.

[190] B. J. Shields, J. Stevens, J. Li, M. Parasram, F. Damani, J. I. M. Alvarado, J. M. Janey, R. P. Adams, A. G. Doyle, Bayesian reaction optimization as a tool for chemical synthesis, Nature 590 (7844) (2021) 89–96.

[191] A. Tran, J. Tranchida, T. Wildey, A. P. Thompson, Multi-fidelity machine-learning with uncertainty quantification and bayesian optimization for materials design: Application to ternary random alloys, The Journal of Chemical Physics 153 (7) (2020).

[192] D. Khatamsaz, B. Vela, P. Singh, D. D. Johnson, D. Allaire, R. Arróyave, Bayesian optimization with active learning of design constraints using an entropy-based approach, npj Computational Materials 9 (1) (2023) 49.

[193] C. K. Williams, C. E. Rasmussen, Gaussian processes for machine learning, Vol. 2, MIT press Cambridge, MA, 2006.

[194] D. Khatamsaz, R. Neuberger, A. M. Roy, S. H. Zadeh, R. Otis, R. Arróyave, A physics informed bayesian optimization approach for material design: application to niti shape memory alloys, npj Computational Materials 9 (1) (2023) 221. doi:10.1038/s41524-023-01173-7.
URL https://doi.org/10.1038/s41524-023-01173-7

[195] M. M. Noack, G. S. Doerk, R. Li, J. K. Streit, R. A. Vaia, K. G. Yager, M. Fukuto, Autonomous materials discovery driven by gaussian process regression with inhomogeneous measurement noise and anisotropic kernels, Scientific Reports 10 (1) (2020) 17663. doi:10.1038/s41598-020-74394-1.
URL https://doi.org/10.1038/s41598-020-74394-1

[196] P. Satria Palar, L. Rizki Zuhal, K. Shimoyama, Gaussian process surrogate model with composite kernel learning for engineering design, AIAA Journal 58 (4) (2020) 1864–1880, doi: 10.2514/1.J058807. doi:10.2514/1.J058807.
URL https://doi.org/10.2514/1.J058807